Confirmatory Appendices

APPENDIX I

ANSI/ANS JET MODEL

I.1 Introduction

Debris generation is the first chronological step in the accident sequence for a postulated high-energy line break. In the idealized case of a double-ended guillotine break (DEGB), high-temperature, high-pressure reactor-cooling fluid may be ejected (from both sides of the broken pipe) that impinges on structures, equipment, piping, insulation, and coatings in the vicinity of the break. The degree of damage induced by the break jets is specific to the materials and structures involved, but the size and shape of the expanding jets and the forces imparted to surrounding objects depend on the thermodynamic conditions of the reactor at the location of the rupture. To maximize the volume of the damage zone (i.e., the zone of influence [ZOI]), it is conservative to consider free expansion of the break jet to ambient conditions with no perturbation, reflection, or truncation by adjacent structures. Spatial volumes of damage potential, as defined by empirical correlations of local jet pressure and observed damage, for example, can then be integrated over the free-jet conditions and remapped into convenient geometries, such as spheres or cones, which approximate the effects of congested reflection without crediting the associated shadowing, jet dispersion, and energy dissipation.

Appendices B, C, and D to the American National Standards Institute (ANSI) guidance for the protection of nuclear power plants against the effects of pipe rupture (ANS88) present one reasonably accessible model for computing pressure contours in an expanding jet. The ANSI model was used for the evaluation of potential damage volumes in the resolution of the boiling-water reactor (BWR) strainer-blockage study (URG96, NRC98). A similar approach suggested for this analysis by ANS88 is a jet model developed at Sandia National Laboratories (WEI83). Both the ANSI and the Sandia models were developed specifically for assessing structural loadings on relatively large targets near the jet centerline, so neither offers a true estimate of local pressures within a freely expanding jet. However, these models can be used with appropriate caution to learn a great deal about the spatial extent of and the thermodynamic conditions present within a high-energy jet.

This appendix presents the equation set needed to evaluate the ANSI model describing two-phase expansion of a jet from a broken high-energy line in a pressurized-water reactor (PWR). To ensure a conservative review of the guidance report (GR), only the conditions related to full separation and full radial offset of a DEGB are developed. The standard presents alternative equations for partial offsets and for longitudinal tears. This discussion is offered to resolve some of the confusion present in the notation of the standard and to provide a self-consistent basis for interpreting computational results relevant to PWR-break conditions. The complexity of the jet model is somewhat beyond the scope of manual evaluation, but several investigators have performed successful spreadsheet calculations for discrete conditions. This appendix used routines (available in ADAMS document ML042640274) developed in MATLAB and FORTRAN for evaluating the jet model as a further guide to implementation and for critical review;

however, this appendix does not provide routines obtained from the National Institute of Standards and Technology (NIST) for evaluating thermodynamic state points.

I.2 Jet-Model Features and Applicability

Despite the apparent complexity of the equation set needed to evaluate the ANSI jet model, it is based on relatively few thermodynamic assumptions and limited comparisons with experimental observation. The bulk of the analytic detail supplies a geometric framework for interpolating jet pressures between assumed or observed transition points. Figure I-1 presents a sample calculation of jet pressure contours for a cold-leg DEGB. Although this calculation represents a relevant bound for evaluation of the GR, to be discussed later, the figure will be used first to introduce geometric features of the model.

The ANSI jet model subdivides the expanding jet into three zones that are delineated by dashed lines in Figure I-1. Zone 1 contains the core region, where it is assumed that liquid extrudes from the pipe under the same stagnation conditions as the upstream reservoir (interior red triangle). Zone 2 represents a zone of continued isentropic expansion, and Zone 3 represents a region of significant mixing with the environment, where the jet boundary is assumed to expand at a fixed, 10-degree, half angle. One group of equations from Appendix C to the standard defines the geometry of the jet envelope, and another group from Appendix D defines the behavior of internal pressure contours. Key geometry features that are determined by the thermodynamic conditions of the break include the length of the core region, the distance to the asymptotic plane between Zones 2 and 3, and the radii of the jet envelope at the transition planes between zones. At the asymptotic plane, the centerline static pressure is assumed to approach the absolute ambient pressure outside of the jet.

Jet pressures provided by the ANSI model must be interpreted as local impingement gauge pressures. This is a property of the pressure field that is relevant to the interpretation of debris generation data; however, a subtle discrepancy exists between the ANSI model predictions and the desired local pressures. Because target materials may reside anywhere within the jet, fluid impingement can occur from a range of angles. Thus, idealized measurements or calculations of free-field impingement pressure should assume that the fluid stagnates (comes to rest) nonisentropically and parallel to the local flow direction. Note that a further subtlety appears here in the distinction between the classical definition of stagnation pressure that is related to the isentropic deceleration of flow along a streamline and the impingement pressure that includes entropy losses resulting from the impact of a fluid on a physical test object. In general, impingement pressures will be higher than stagnation pressures, but the two terms may be used synonymously at times in this appendix.

In contrast to the desired local impingement pressure, the ANSI model appears to be concerned with total force loadings across relatively large objects placed near the jet centerline. Appendix D to the standard states that the pressure recovered on a target is related to the component of the flow perpendicular to the target and, because of the diverging flow in an expanding jet, the pressure distribution on a large flat target will decrease in the radial direction. The pressure equations in the standard produce exactly this effect, and a brief allusion is made to a comparison of the predicted pressures with data taken across the face of large targets placed perpendicular to the jet. The standard gives further cautionary notes against applying the pressure equations to predict forces

on small objects near the edges of the jet where flow velocities are clearly not parallel to the centerline.

These attributes of the model suggest that calculated pressures represent jet impingement conditions that would be experienced in a direction parallel to the midline only. Actual streamlines in a rapidly expanding jet must have a significant radial velocity component to create the characteristic envelope shown in Figure I-1; in a sense, the predicted pressures represent only the longitudinal component of the local, momentum-dominated, total jet pressure. The implication of this interpretation is that true local impingement pressures, as measured normal to realistic flow directions in the jet, may be underestimated, particularly in Zones 1 and 2, where radial expansion is greatest.

Although a computed pressure isobar may be smaller in radius than that of the corresponding local impingement pressure that is desired for debris generation estimates, it may also be longer in the downstream direction. Comparative elongation of isobars from the jet model occurs because the entire mass flux ejected from the break is assumed to pass through the jet cross section at the asymptotic plane. Thus, the forward momentum of the jet is maximized in a manner that would be considered conservative for structural loading calculations. Unrealistic isobar elongation may also be predicted because the jet centerline pressure equation for Zone 3 is inherently unbounded; the centerline gauge pressure only falls to zero as the jet diameter grows infinitely large at infinite distance. The net effect on isobar volume of these disparities between the ANSI model and the desired free-expansion impingement pressures is impossible to quantify without a complete understanding of the experimental measurements on which the model is based; however, the mathematical properties of the pressure equations are certain to exaggerate the length, and hence the volume, of low-pressure isobars.

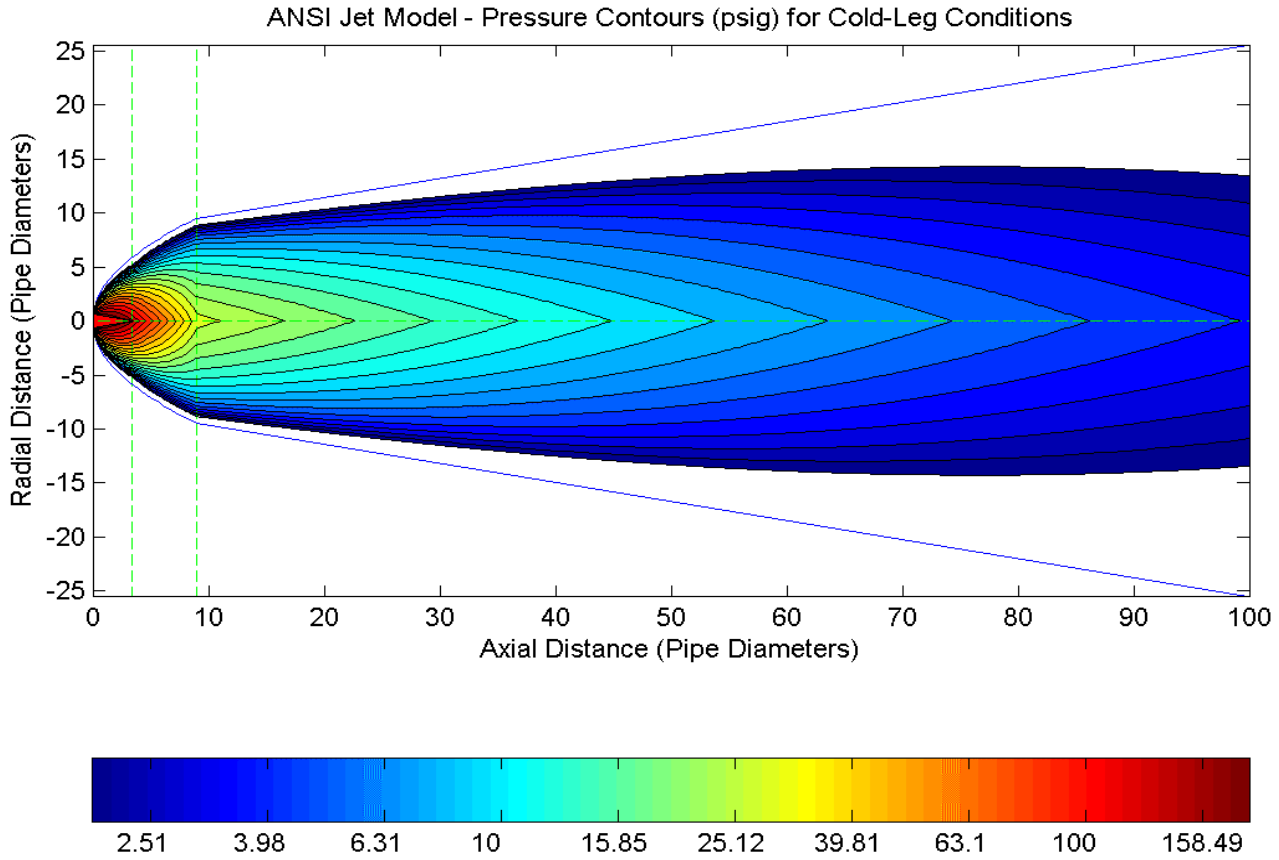

Figure I-1. ANSI Jet-Model Stagnation Pressures for PWR Cold-Leg Break Conditions (530 °F, 2250 psia)

I.3 Jet-Model Equation Set

I.3.1 Fundamentals

Equations developed in the standard frequently refer to four distinct thermodynamic state points:

(1) stagnation conditions of the fluid in the upstream reservoir denoted by subscript "0" (zero)

(2) conditions at the exit plane of the pipe denoted by subscript "e"

(3) conditions at any point in the jet denoted either with subscript "j" or with no subscript at all

(4) conditions at the asymptotic plane denoted by subscript "a"

These conventions are rigidly applied in the following development to resolve some notation inconsistencies found in the standard. Unless otherwise noted, pressures will refer to the absolute thermodynamic static pressure of the fluid. The first exception to this rule has already been mentioned—that is, the jet-pressure equations that define the local, gauge, longitudinal, and impingement pressure.

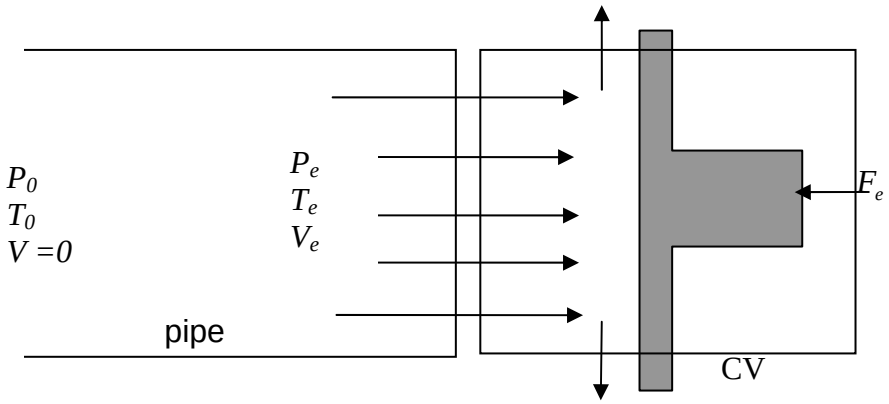

Figure I-2. Control-Volume Force Balance on a Rigid Plate near the Outlet

One of the more fundamental relations in the model is actually presented near the end of the standard in Appendix D; it defines the total thrust (force) of the jet at the outlet. If a rigid plate were placed near the outlet, as shown in Figure I-2, the force balance on a control volume (CV) must consider both the static pressures and the rate of change of momentum acting on the boundary. If mass exits the control volume in a symmetric pattern at uniform velocity, the only possible force imbalance is in the x direction. The force on a plate near the exit is then

$$F_e = P_e A_e - P_{amb} A_e + \frac{1}{g_c}\frac{d}{dt}(m_e v_e) = (P_e - P_{amb})A_e + \frac{1}{g_c}\left[\left(\frac{d}{dt}m_e\right)v_e + m_e\left(\frac{d}{dt}v_e\right)\right] \qquad \text{(I-1)}$$

where

P_e = the fluid pressure at the exit plane,

P_{amb} = the ambient pressure in containment,

A_e = the area of the break, and

m_e = the mass entering the control volume at velocity v_e.

The force-to-mass conversion factor, g_c, equals 32.2 lbm·ft/lbf·s^2 in English units. Mass enters the control volume at constant velocity $\left(\frac{d}{dt}v_e = 0\right)$ at a rate of $\frac{d}{dt}m_e = \rho_e v_e A_e$, where ρ_e is the fluid density at the exit. Thus, the total thrust generated at the exit plane is

$$F_e = (P_e - P_{amb})A_e + \frac{1}{g_c}\rho_e v_e^2 A_e \qquad \text{(I-2)}$$

Substitution of $G_e = \rho_e v_e$ for the critical mass flux crossing the exit plane yields

$$F_e = \left[(P_e - P_{amb}) + \frac{G_e^2}{g_c \rho_e}\right]A_e \qquad \text{(I-3)}$$

where the first term represents force applied by the static pressure of the fluid and the second term represents force imparted by the momentum of the fluid. The ambient pressure is often assumed to be zero to maximize the available jet thrust conservatively.

Division of equation (I-2) or (I-3) by the exit area suggests an effective, or area-averaged, jet pressure of $\overline{P_e} = F_e / A_e$. This effective pressure will be greater than the classical stagnation pressure at the exit, which is defined by Bernoulli's equation as $P_e^{stag} = P_e^{static} + \frac{1}{2g_c}\rho_e v_e^2$ because the derivation of Bernoulli's law requires that the fluid be brought to rest in an idealized, reversible manner. Jet impingement on a body is a highly anisentropic process. For an incompressible fluid, the static pressure at the exit equals the ambient pressure, and if friction losses in piping between the reservoir and the break can be neglected, the stagnation pressure at the exit equals the initial pressure. Under these conditions, Bernoulli's equation can be written as

$$\frac{1}{g_c}\rho_e v_e^2 = 2(P_0 - P_{amb}) \qquad \text{(I-4)}$$

Equations (I-2) and (I-3) are often simplified as $F_e = C_T P_0 A_e$, where P_0 is the upstream stagnation pressure and C_T is the thrust coefficient defined by comparison to be

$$C_T = \frac{1}{P_0}\left[\frac{1}{g_c}\rho_e v_e^2 + \left(P_e - P_{amb}\right)\right] = \frac{1}{P_0}\left[\frac{G_e^2}{g_c \rho_e} + \left(P_e - P_{amb}\right)\right] \quad \text{(I-5)}$$

Equation (I-5) emphasizes that the fluid properties that exist at the exit plane determine the correlation between upstream stagnation pressure and the thrust coefficient. Several alternative models are available to describe the thermodynamic transitions occurring in a high-energy fluid that is expanding and accelerating, which, in turn, determine the exit density and the critical mass flux. It is very important that the specification of C_T be consistent with the models used to evaluate G_e and ρ_e. It should be noted that the standard uses inconsistent notation for the thrust coefficient (e.g., C_T, C_{T_e}, $C_{T_e}^*$). All forms must refer to a single numeric value, if the pressure equations are to be piecewise continuous between jet zones.

Under the conditions of zero friction loss and incompressible flow (solid liquid with no vapor fraction where $P_e = P_{amb}$), equation (I-4) can be substituted into equation (I-5) to obtain a theoretical maximum value of $C_T = 2.0$ when ambient pressure is neglected. By treating steam as a perfect gas under isentropic flow to obtain the exit velocity, Shapiro (SHA53) derives a lower theoretical limit of $C_T = 1.26$. Any numeric evaluation of equation (I-5) using water property tables to derive G_e and ρ_e should be compared to these limits. Although it is clearly most conservative to apply the liquid limit for all state points, numerical evaluation of equation (I-5) using water tables is sufficiently robust to permit this refinement. Section I.4 of this appendix discusses recommendations for computing the thrust coefficient and provides convenient reference figures.

I.3.2 Jet-Envelope Geometry

The thermodynamic conditions upstream of the break dictate the shape and size of the jet envelope predicted by the ANSI model. Except where noted, spatial distances are represented in dimensionless multiples of the broken-pipe inside diameter, D_e. Jet boundaries (and pressure contours) can be scaled in this manner because the equation set is linear with respect to pipe diameter. Linearity can be proven rigorously by factoring and eliminating terms of D_e in every equation. In general, because of potential nonlinearities, it is not sufficient to evaluate a complicated dimensional equation set at a unit value of a candidate scaling parameter and then to assume that the unit result can be multiplied by any desired value of that parameter. To recover physical quantities for a particular pipe size, dimensionless distances must be multiplied by D_e, dimensionless areas must be multiplied by D_e^2, etc.

The distance of extrusion by the jet core is

$$L_c = 0.26\sqrt{\Delta T_{sub}} + 0.5 \quad \text{(I-6)}$$

where ΔT_{sub} is the degree of subcooling (°F) upstream of the break location (i.e., the difference between the saturation temperature T_{sat} at the system pressure P_0 and the system temperature T_0). The interior red triangle in Figure I-1 shows the jet core. Note that L_c takes on a value of 0.5 for saturated or superheated conditions. In addition, if $L_c > L_a$, then the distance to the asymptotic plane defined below, L_c should be set to zero and the jet pressure should be assumed to be uniform across the break area at a value of $\overline{P}_j = \left(F_e / A_e\right) / C_T$, where the ratio F_e / A_e is computed from equation (I-2) or (I-3). This can occur for low-pressure nonexpanding jets. A jet can be treated as nonexpanding when the initial temperature of a liquid reservoir is less than the saturation temperature at P_{amb} or the initial pressure of a gas reservoir is equal to ambient pressure, $P_0 = P_{amb}$.

The diameter of the jet at the exit plane is defined to be

$$D_{je} = \sqrt{C_T} \tag{I-7}$$

which is slightly larger than the diameter of the pipe because $1.26 \le C_T \le 2.0$.

The diameter of the jet at the asymptotic plane (Zone 2 to Zone 3 boundary) is defined by the relation

$$D_a^2 = \frac{G_e^2}{g_c \rho_a C_T P_0} \tag{I-8}$$

where ρ_a is the homogeneous fluid density at the centerline distance to this plane, which is given by

$$L_a = \frac{1}{2}\left(D_a - 1\right) \tag{I-9}$$

Note that some care must be taken to keep pressure and mass flux dimensionally consistent in equation (I-8). The density ρ_a is to be evaluated at a state point defined by the system enthalpy h_0 and an asymptotic-plane static pressure defined by

$$P_a = \left\{1 - 0.5\left(1 - \frac{2P_{amb}}{P_o}\right) f\left(h_o\right)\right\} P_{amb} \tag{I-10}$$

where

$$f(h_0) = \sqrt{0.1 + \frac{h_o - h_f}{h_{fg}}} \text{ for } \frac{h_o - h_f}{h_{fg}} > -0.1, \text{ and } f(h_0) = 0 \text{ otherwise.} \qquad \text{(I-11)}$$

Within the condition stated by equation (I-11), h_f and h_g are the saturated fluid enthalpy and saturated vapor enthalpy at P_0, respectively, and $h_{fg} = h_g - h_f$ is the heat of vaporization. Further conditions on equation (I-10) are that if the ratio $P_{amb} / P_0 > 1/2$, then it should be set equal to 1/2 and that, as a static pressure, $P_a \geq 0$.

The first criterion on $f(h_0)$ simply checks whether the initial quality $x_0 = \frac{h_o - h_f}{h_{fg}}$ is greater than negative 10 percent. When considered as a whole, these conditions imply that $0 \leq P_a \leq P_{amb}$. If the initial fluid is more than 10 percent subcooled, the jet static pressure equals ambient pressure at the asymptotic plane. If the jet is less than 10 percent subcooled, the jet static pressure at the asymptotic plane can be lower than ambient pressure. Equation (I-10) suggests that the asymptotic plane is placed at the distance where the jet static pressure approaches ambient pressure. The distance to this plane given by equation (I-9) may simply have been chosen by geometric comparison with observed jets.

The state point defined by the asymptotic pressure P_a and the system enthalpy h_0 may be a two-phase condition. In this case, it is necessary to evaluate the asymptotic density ρ_a using the quality $x_a = \frac{h_o - h_{fa}}{h_{ga} - h_{fa}}$, where h_{fa} and h_{ga} are the saturated fluid and vapor enthalpies at P_a, respectively. Then, $\rho_a = \left[\frac{x_a}{\rho_{ga}} + \frac{1 - x_a}{\rho_{fa}} \right]^{-1}$, where ρ_{fa} and ρ_{ga} are the saturated fluid and vapor densities at P_a, respectively. Automated steam tables generally give mixture densities directly for a two-phase state point, so this complication may be unnecessary.

The similarity of terms in equation (I-8) to the force-balance equations derived in the previous section suggests a different interpretation for the asymptotic plane. For convenient reference, the jet diameter at the asymptotic plane is again given by

$$D_a^2 = \frac{G_e^2}{g_c \rho_a C_T P_0} \qquad \text{(I-12)}$$

Given the discussion following equation (I-3) and the definition of the thrust coefficient, the factors $C_T P_0$ in equation (I-12) are immediately recognized as $\overline{P_e} = F_e / A_e$, the average total jet pressure at the exit. If a relation similar to equation (I-3) is written to

describe the area-averaged pressure across the jet cross section at the asymptotic plane,

$$\overline{P}_a = \frac{F_a}{A_a} = \left[\left(P_a - P_{amb} \right) + \frac{G_e^2}{g_c \rho_a} \right] \tag{I-13}$$

then the term $G_e^2 / g_c \rho_a$ in equation (I-12) is recognized to be $\overline{P}_a - \left(P_a - P_{amb} \right)$. If the static pressure at the asymptotic plane P_a is not much different than the ambient pressure P_{amb}, then equation (I-12) reduces to the ratio of average pressures computed over the jet cross section at the asymptotic plane and over the jet cross section at the exit,

$$D_a^2 = \frac{F_a / A_a}{F_e / A_e} = \frac{\overline{P}_a}{\overline{P}_e} \tag{I-14}$$

Writing explicitly the definition of the dimensionless asymptotic-plane area as $D_a^2 = \frac{A_a}{A_e}$ illustrates that the diameter of the jet given by equation (I-8) has been chosen at the point where the ratio of average pressures approaches the ratio of cross sectional areas, and for this to be true, the total force across each area must be the same. Hence, the ANSI model implicitly assumes that the jet force available at the outlet is conserved across the jet cross section at the asymptotic plane. At this distance, the jet is presumed to begin interacting with the environment.* This development also shows that the ANSI model projects the entire mass flux across the asymptotic plane rather than following more realistic streamlines across the jet boundary in Zones 1 and 2. Section I.4 derives equation (I-8) more rigorously to further emphasize these points.

The remainder of the jet envelope is simply interpolated as a function of centerline distance *L* between the transition diameters discussed above. Within Zone 1, the diameter of the jet core is given by

$$D_c = \sqrt{C_T} \left(1 - \frac{L}{L_c} \right) \tag{I-15}$$

For Zones 1 and 2 $\left(0 < L \le L_a \right)$, the jet diameter is given by

$$D_j^2 = \left[1 + \frac{L}{L_a} \left(\frac{D_a^2}{D_{je}^2} - 1 \right) \right] D_{je}^2 \tag{I-16}$$

* This observation was derived from the jet equations and is not expounded as part of any derivation in the standard. It is simply an implication of the definitions.

In Zone 3 $\left(L > L_a\right)$, the jet diameter expands at a 10-degree half angle beginning from the diameter at the asymptotic plane. The Zone-3 diameter is specified by

$$D_j^2 = \left[1 + \frac{2\left(L - L_a\right)}{D_a}\tan\left(10°\right)\right]^2 D_a^2 \quad . \tag{I-17}$$

I.3.3 Jet Pressures

Pressure contours also appear to be interpolated from a limited number of geometric reference points, but the basis for this interpolation is not evident from the standard. It can be shown that all equations are piecewise continuous at the separation planes between zones; however, no effort was made to match first-derivative slopes. This deficiency admits the possibility of "kinks" in the contours, as observed in Figure I-1 across the boundary between Zones 2 and 3. Pressure contours in Zone 1 $\left(0 \le L \le L_c\right)$ depend on the following discriminant. If

$$D_j^2 + 2D_j D_c + 3D_c^2 \le 6C_T\,, \tag{I-18}$$

then the jet pressures are given as a function of radius $\left(r_c < r \le r_j\right)$ for jet diameters $D_j = 2r_j$ as

$$P_j = \left(\frac{D_j - 2r}{D_j - D_c}\right)\left[1 - \frac{2\left(D_j^2 + D_j D_c + D_c^2 - 3C_T\right)}{D_j^2 - D_c^2}\left(\frac{2r - D_c}{D_j - D_c}\right)\right]P_0\,. \tag{I-19}$$

Otherwise,

$$P_j = \left(\frac{D_j - 2r}{D_j - D_c}\right)^2\left[\frac{6\left(C_T - D_c^2\right)}{\left(D_j - D_c\right)\left(D_j + 3D_c\right)}\right]P_0\,. \tag{I-20}$$

It is important to note that the leading term $\left(D_j - 2r\right)$ vanishes in both equations (I-19) and (I-20) as the radius approaches the jet envelope where the absolute pressure equals P_{amb}. Therefore, evaluations of P_j must be interpreted as gauge pressures. In equation (I-19), the term $\left(\frac{2r - D_c}{D_j - D_c}\right)$ ensures that the jet pressure matches P_0 on the boundary of the core. Equation (I-20) provides no similar constraint, so there will be a sharp discontinuity in pressure at the boundary of the jet core when this condition is invoked, as shown in Figure I-1. Equations (I-19) and (I-20) were not intended to be evaluated inside of the core region. Within the core, the system stagnation conditions are presumed to hold.

In Zones 2 and 3, jet pressures are parameterized in terms of the jet centerline pressure P_{jc}. In Zone 2 $\left(L_c < L \le L_a\right)$,

$$P_{jc} = \left\{ F_c - \left(F_c - \frac{3C_T}{D_a^2} \right) \frac{L_a}{L} \frac{\left(L - L_c\right)}{\left(L_a - L_c\right)} \right\} P_0 , \tag{I-21}$$

where the parameter $F_c = 1.0$, if $D_j^2 \le 6C_T$ at distance L_c, and $F_c = 6C_T / D_j^2$ otherwise. When $L = L_c$, equation (I-21) reduces to $P_{jc} = F_c P_0$. If $F_c = 1.0$, the centerline pressure will match the assumed pressure in the core region, but otherwise, there will again be a discontinuity. Given the centerline pressure, jet pressures in Zone 2 are specified by

$$P_j = \left(1 - \frac{2r}{D_j} \right) \left\{ 1 - 2\left(\frac{2r}{Dj} \right) \left[1 - \frac{3C_T}{D_j^2} \frac{P_0}{P_{jc}} \right] \right\} P_{jc} . \tag{I-22}$$

It can be shown by integration that equation (I-22) is essentially a geometric rather than physical condition—it leads to full recovery of the jet force anywhere in Zone 2 regardless of the value assigned to the jet diameter. In Zone 3, centerline pressures are given by

$$P_{jc} = \frac{3C_T P_0}{D_a^2 \left[1 + \frac{2\left(L - L_a\right)}{D_a} \tan\left(10°\right) \right]^2} \tag{I-23}$$

and jet pressures are given by

$$P_j = \left(\frac{D_j - 2r}{D_j} \right) P_{jc} . \tag{I-24}$$

Pressures on the transition between Zones 2 and 3 are piecewise continuous, including on the centerline.

I.3.4 Pressure-Contour Characteristic Equations

Equations presented in the previous section can be used to evaluate longitudinal impingement pressures at any location in the jet. However, in the present forms, they are not particularly convenient for identifying geometric characteristics, such as isobar boundaries. Similarly, when numerically computing volumes under a given isobar, it is convenient to know the downstream range of the contour, which always begins at $L = 0$ and terminates in a cusp on the centerline at some distance, $L = L_t\left(P_j\right)$. The ANSI standard does not develop the relationships presented in this section; they are offered to facilitate some of the many practical details involved with implementing the standard.

Figure I-1 illustrates the typical behavior of jet-pressure isobars generated by the ANSI model. The isobars outlined in black represent lines of constant pressure that can be

found by solving the pressure equations (I-19), (I-20), (I-22), and (I-24) for the radii at a constant pressure, P_j. The jet diameter, D_j, implicitly specifies the downstream distance L. Each pressure equation can be reduced to a general quadratic expression for the radius of the form $Ar^2 + Br + C = 0$.

The coefficients from equation (I-19) for Zone 1 are

$$A = 4H\ ,\quad B = -2\left[1 + H\left(D_j + D_c\right)\right], \text{ and } C = D_j + HD_jD_c + \left(D_c - D_j\right)\frac{P_j}{P_0}, \qquad \text{(I-25)}$$

where

$$H = 2\frac{\left(D_j^2 + D_jD_c + D_c^2 - 3C_T\right)}{\left(D_j^2 - D_c^2\right)\left(D_j - D_c\right)}. \qquad \text{(I-26)}$$

The coefficients from equation (I-20) for Zone 1 are

$$A = 4\ ,\ B = -4D_j\text{, and } C = D_j^2 - \left(D_j - D_c\right)^2\frac{P_j}{P_0}I\ , \qquad \text{(I-27)}$$

where

$$I = \frac{6\left(C_T - D_c^2\right)}{\left(D_j - D_c\right)\left(D_j + 3D_c\right)}. \qquad \text{(I-28)}$$

A special case occurs in Zone 1 at $L = 0$, where $D_j = D_c$ and $r = D_j/2 = D_c/2$ for all P_j.

Equation (I-22) yields the following coefficients for Zone 2:

$$A = 8\frac{J}{D_j^2}\ ,\ B = -\left(\frac{2}{D_j} + \frac{4J}{D_j}\right)\text{, and } C = 1 - \frac{P_j}{P_{jc}}\text{, where } J = \left(1 - \frac{3C_T}{D_j^2}\frac{P_0}{P_{jc}}\right). \qquad \text{(I-29)}$$

Finally, equation (I-24) yields the following coefficients for Zone 3:

$$A = 0\ ,\ B = -2/D_j\text{, and } C = 1 - \frac{P_j}{P_{jc}}. \qquad \text{(I-30)}$$

The analytic solution for the radius in Zone 3 is

$$r = \frac{1}{2} D_j \left(1 - \frac{P_j}{P_{jc}} \right). \tag{I-31}$$

The sharp tip of each contour shown in Figure I-1 is another nonphysical feature of the ANSI model that arises from a lack of attention to matching spatial first derivatives. It might be expected that each isobar is smoothly bounded and has infinite slope at the terminal point, especially at very low pressures where the jet returns to ambient conditions. It is helpful to know the distance to the terminal point of each contour for iterative integration of spatial volumes. These points can be found by solving the centerline pressure equations (I-21) and (I-23) for distances L_t corresponding to the desired pressure. Note that Zone 1 has no terminal points except for the jet core.

For Zone 2, equation (I-21) yields the relation

$$L_t = \frac{L_c}{1 - \dfrac{L_a - L_c}{R L_a} \left(F_c - \dfrac{P_j}{P_0} \right)}, \tag{I-32}$$

where

$$R = F_c - \frac{3 C_T}{D_a^2}, \tag{I-33}$$

and for Zone 3, equation (I-23) yields the relation

$$L_t = \frac{1}{2} \left[\left(\frac{3 C_T P_0}{D_a^2 P_j} \right)^{1/2} - 1 \right] \frac{D_a}{\tan(10°)} + L_a . \tag{I-34}$$

One remaining practicality is the numerical integration of pressure isobars defined by equations (25), (27), (29), and (31). If these equations are evaluated at a set of discrete distances, L_i, the corresponding radii, r_i, define adjacent conical frusta with unique slopes, as shown in Figure I-3. The analytic formula for the frustum of a cone is given by

$$V_i = \pi \left[\frac{1}{3} m_i^2 L^3 + m_i \left(r_{i+1} - m_i L_{i+1} \right) L^2 + \left(m_i^2 L_{i+1}^2 - 2 r_{i+1} m_i L_{i+1} + r_{i+1}^2 \right) L \right]_{L_i}^{L_{i+1}} \tag{I-35}$$

where the linear slope of the sides of the conical segment is $m = \dfrac{r_{i+1} - r_i}{L_{i+1} - L_i}$. The total volume under the isobar is approximated by the sum $V_{isobar} = \sum V_i$ and can be refined to any desired accuracy by evaluating the pressure-isobar equations at finer resolution.

The total volume of an isobar should be multiplied by a factor of 2 when double-ended breaks of equivalent upstream pressure are considered and, finally, converted to a volume-equivalent sphere by the formula

$$R_{sphere} = \left(\frac{3}{4\pi} V_{isobar} \right)^{1/3} . \qquad \text{(I-36)}$$

I.4 Derivation of Asymptotic-Plane Area

To obtain equation (I-8) for the jet diameter D_a at the asymptotic plane, a force balance is applied to the control volume shown in

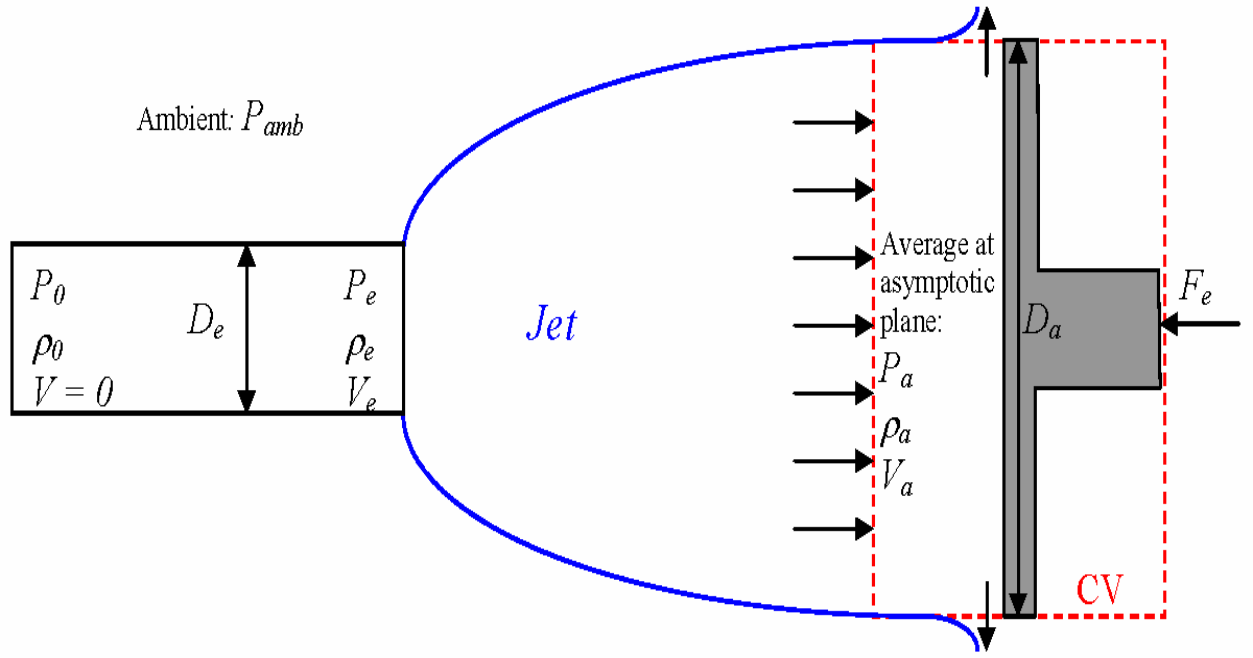

Figure I-4 in a manner analogous to the derivation of the thrust force given by equation (I-2). In the figure, a plate is positioned normal to the flow at the asymptotic plane. The force required to hold the plate in static equilibrium is notated F_e. The fluid deflected by the plate is assumed to exit the control volume isotropically in a plane oriented parallel to the face of the plate.

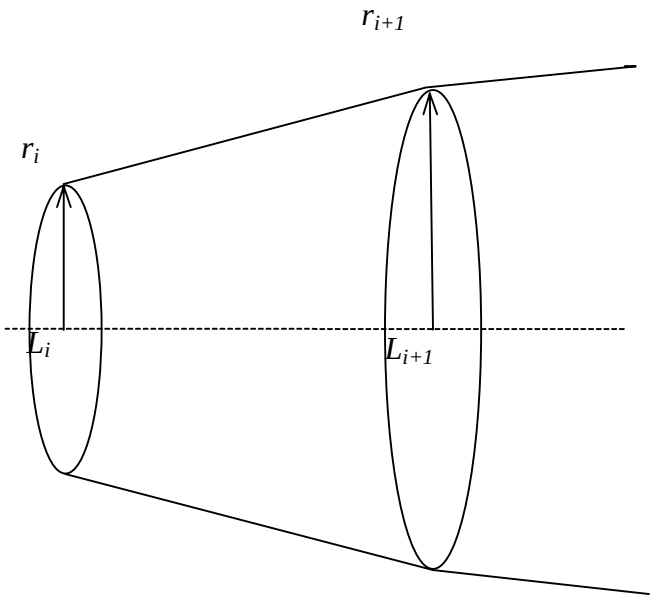

Figure I-3. Linear Segmentation of Jet Cross Sections for Numerical Volume Integration

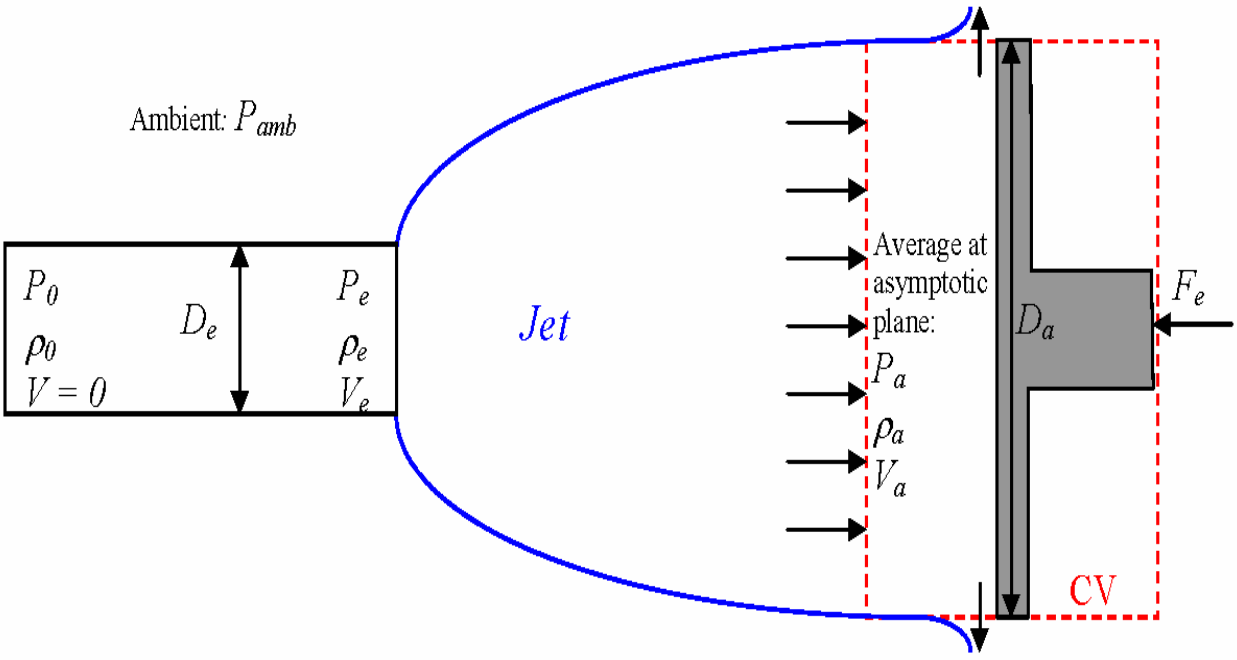

Figure I-4. Control-Volume Force Balance on a Rigid Plate at the Asymptotic Plane Used to Derive Equation (C-3) in the ANSI Standard

It is assumed in Appendix C to the ANSI standard (p. 52) that the fluid does not begin to interact with the surrounding environment until after it crosses the asymptotic plane. Hence, no energy is supplied to or removed from the jet in the region upstream of the control volume in

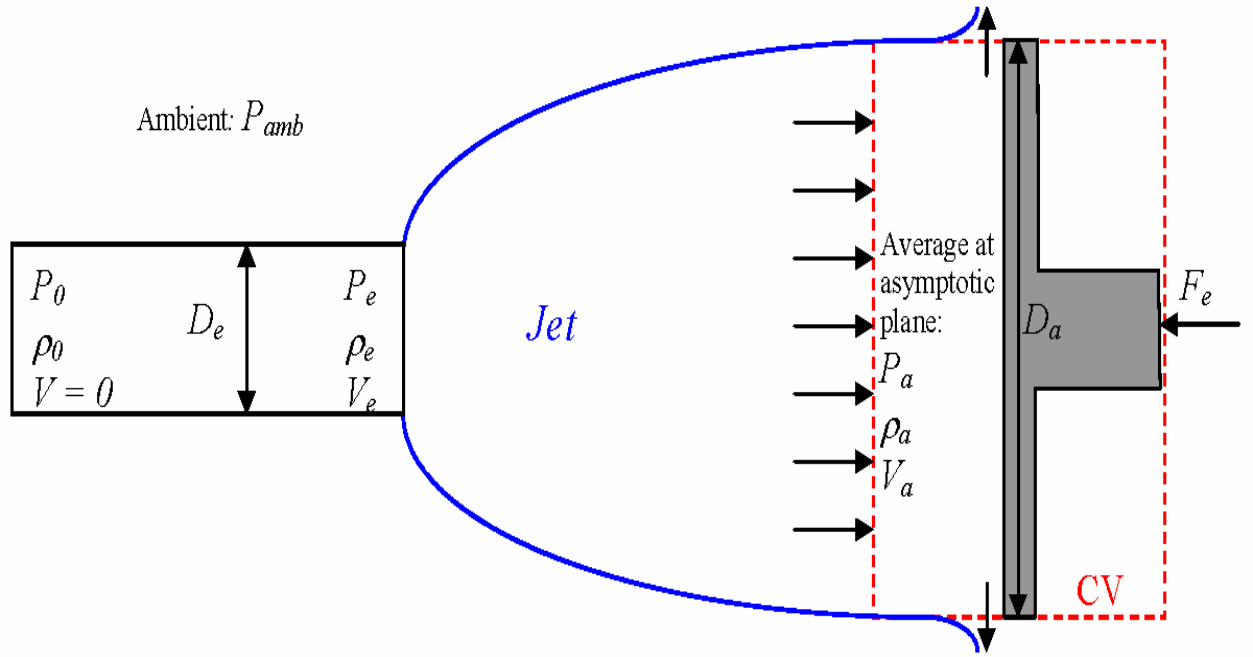

Figure I-4. Therefore, the entire jet force will be recovered on a target at this distance.

The jet characteristics at the asymptotic plane—fluid density ρ_a, velocity v_a, and static pressure P_a—are not expected to be uniform, so to render the force balance for the control volume tractable, these properties are averaged over the jet cross section. The force balance in the direction of the jet flow may hence be written as

$$F_e = (P_a - P_{amb})A_a + \frac{1}{g_c}\left(v_a \frac{d}{dt} m_a + m_a \frac{d}{dt} v_a\right), \tag{I-37}$$

where $A_a = \pi D_a^2 / 4$ is the jet area at the asymptotic plane and m_a is the mass of the fluid located within the control volume.

For steady flow, $dv_a / dt = 0$. The rate at which mass enters the control volume, dm_a / dt, is simply the total mass flow crossing the asymptotic plane and is given by

$$\frac{dm_a}{dt} = \rho_a v_a A_a. \tag{I-38}$$

Hence, the force balance simplifies to

$$F_e = (P_a - P_{amb})A_a + \frac{1}{g_c}\rho_a v_a^2 A_a. \tag{I-39}$$

Because no mass escapes the jet between the break location and the asymptotic plane, the mass flow rates at the break and at the asymptotic plane must be equal, that is,

$$\rho_a v_a A_a = \rho_e v_e A_e. \tag{I-40}$$

This relation may be employed to eliminate v_a in the force balance.

As mentioned in the discussion following equation (I-11), the static pressure at the asymptotic plane is generally taken to be equal to P_{amb}. Setting P_a equal to P_{amb} yields

$$F_e = \frac{1}{g_c}\frac{\rho_e^2 v_e^2 A_e^2}{\rho_a A_a}. \tag{I-41}$$

Because the full jet thrust force is recovered, this evaluation of F_e may be set equal to that obtained in equation (I-2) to give the result

$$\frac{A_a}{A_e} = \frac{\rho_e^2 v_e^2}{g_c \rho_a} \cdot \frac{1}{(P_e - P_{amb}) + \frac{1}{g_c}\rho_e v_e^2}. \tag{I-42}$$

The second fraction in this equation is recognized by comparison with equation (I-5) as equal to $1/(C_T P_0)$. Making use of the mass flux definition, $G_e = \rho_e v_e$, leads to the expression for the jet area at the asymptotic plane given in the standard,

$$\frac{A_a}{A_e} = \frac{G_e^2}{g_c \rho_a C_T P_0}. \tag{I-43}$$

The standard recommends evaluation of the density ρ_a at the asymptotic plane using the local static pressure P_a and the system stagnation enthalpy h_0, rather than the local static enthalpy h_a. Therefore, it is implicitly assumed that the dynamic enthalpy at the asymptotic plane, $v_a^2/2$, is small. This assumption is questionable given that v_a is generally not small, even for the large asymptotic area obtained by the method of calculation of the standard. For the sample case considered earlier (P_0 = 2250 psia, T_0 = 530°F, h_0 = 522 Btu/lbm upstream stagnation conditions), following the recommendations of the standard, the plane-averaged fluid density at the asymptotic plane is 0.106 lbm/ft^3 and the averaged fluid velocity is 670 ft/s. One would then compute $v_a^2/2 \approx$ 9.0 Btu/lbm, a nonnegligible fraction of the initial enthalpy. The

calculational simplicity achieved by use of upstream stagnation conditions, rather than the local static conditions for thermodynamic evaluations, is therefore of doubtful value.

A further inconsistency is noted in the development of the asymptotic plane area because P_a in the ANSI jet model, as governed by equation (I-10), is not always equal to P_{amb}, yet the asymptotic plane area is always computed as if this were the case. For slightly subcooled, saturated, or two-phase upstream conditions, application of equation (I-10) leads to a value for P_a that is less than P_{amb}. Although the standard does not document the physical reasoning behind equation (I-10), it appears to correct for cases in which the dynamic enthalpy is nonnegligible. This development further confirms that only longitudinal pressures are computed for P_{jet}, at least at the asymptotic plane, and probably everywhere within the jet envelope.

I.5 Critical Flow Models

I.5.1 Discharge Mass Flux

Results produced by the jet model are sensitive to the value assigned to the mass flux discharged from the break plane, G_e (lbm/ft^2/s). The area of the jet at the asymptotic plane A_a (ft^2) (i.e., the cross sectional area reached by the jet following free (isentropic) expansion), is proportional to G_e^2. Thus, Figures C-4 and C-5 in the standard indirectly specify G_e and plot the ratio of the asymptotic area to the break plane area A_a / A_e for upstream conditions ranging from 50 °F subcooled liquid to saturated vapor. Aside from difficulties inherent in recovering numerical values from coarsely resolved plots, use of these figures is not recommended for the following two reasons:

(1) The range of upstream stagnation conditions covered by the plot—extending only to 50°F subcooling—is insufficient. Typical cold-leg conditions in a PWR might entail subcooling of 100°F or more.

(2) The origin of the results is unclear. Which model was used to evaluate the relevant mass fluxes and thrust coefficients? Without this information, there can be no confidence that the rest of the model will be applied in a self-consistent manner.

Therefore, this analysis strongly concurs with the recommendation given in the ANSI standard (p. 57) that a two-phase critical flow model be employed to evaluate G_e. The standard cites two models that are in widespread use, the homogeneous equilibrium model (HEM)[†] and the Henry-Fauske model (HEN71). The standard provides a loose recommendation regarding the applicability of the models as a function of upstream stagnation properties—the HEM for saturated or two-phase and Henry-Fauske for subcooled conditions.

[†] For a discussion of practical considerations surrounding implementation of the HEM, as well as a tabulation of results for a wide range of upstream conditions, see HAL80.

Several pitfalls await a naïve application of this guidance. To facilitate the exposition of these pitfalls, it is useful first to provide a simplified description of the physics inherent in each of the models.

The HEM assumes the phases to be in thermodynamic equilibrium and to remain well mixed. The relative velocity between the phases is therefore assumed to be zero. External heat transfer, wall roughness, and other interactions with the environment are neglected so that the expansion is isentropic.

Given these assumptions, the first law of thermodynamics is applied to the homogenized fluid. Combined with the definition of the mass flux, the first law yields an expression for G_e in terms of the mixture's static properties at the choked point. The critical mass flux is defined as the value of G_e that maximizes this expression. Numerical solution of the HEM is thus an iterative process, entailing a search over the space of static state points that preserve the upstream stagnation entropy.

The Henry-Fauske model preserves some of the assumptions made under the HEM, namely that the mass flux may be expressed as a function of the thermodynamic state at the throat, that the critical mass flux can be obtained by maximizing this function, and that the expansion is isentropic. However, Henry and Fauske argue that the assumptions of homogeneous mixing and thermodynamic equilibrium during the expansion are unrealistic given the short time scales involved. Rather, interphase mass transfer is constrained such that the quality, x_t, at the throat is equal to the upstream stagnation quality, x_0. Heat transfer during the expansion is also assumed negligible; the liquid-phase temperature T_{ft} at the throat is held fixed at the upstream liquid temperature, T_{f0}. The temperature of the vapor phase, if it is present, is allowed to vary. The heat- and mass-transfer rates at the throat are treated as significant, and expressions for these are developed assuming polytropic vapor behavior.

In practice, the Henry-Fauske model is implemented by solving a transcendental equation for the static pressure at the throat that maximizes mass flux. Both Henry-Fauske and the HEM are evaluated through iterative procedures, with thermodynamic properties queried upon each iteration. Therefore, the models were coded as a series of FORTRAN subroutines, driven by a MATLAB control function, that directly couple with the FORTRAN implementation of the NIST/American Society of Mechanical Engineers (ASME) steam tables (HAR96) when fluid properties are required. The results obtained from the software were successfully validated against those presented in HAL80 and HEN71**.** These programmed routines allow a thorough assessment of the practical ramifications of using each model within the ANSI jet-modeling framework.

The standard does not provide guidance with regard to critical flow modeling for superheated conditions. The simplest approach would be to treat the steam as an ideal gas and apply the appropriate equation of state. This treatment was attempted and found to be highly inadvisable for the slightly superheated states that are of most relevance to the present application. Two qualitative observations support this conclusion. First, when the upstream superheat is small, the flow at the choked location is in fact two phase; second, slightly superheated, high-pressure steam does not exhibit the typically assumed idealized properties (e.g., a specific heat ratio of 1.3), so that

transitions evaluated using the ideal gas law would not preserve entropy. These considerations lead to the recommendation that the HEM be used treat the superheated state points that may arise in this application.

As mentioned above, the standard does provide guidance for two-phase and single-phase liquid stagnation state points. Specifically, it recommends the use of HEM for saturated and Henry-Fauske for subcooled upstream conditions. This appendix recommends using the Henry-Fauske model for both regimes. This recommendation stems from several considerations, as outlined below.

Critical mass fluxes predicted by the HEM and Henry-Fauske models exhibit their most significant disagreement at precisely the transition point recommended in the standard (i.e., for saturated-liquid upstream conditions). **Error! Reference source not found.** and Figure I-6 provide contour plots of G_e, as obtained from the two models for subcooled vessel stagnation conditions. In figures showing flow properties for subcooled state points, the stagnation temperature is varied on the x axis and pressure on the y axis. The regions between contour lines of constant G_e are shaded for ease of delineation. Because the domain of validity of the flow models does not extend to superheated conditions, pressure and temperature combinations that lie within this regime are blanked out on the plots. Figure I-7 and Figure I-8 show mass fluxes for saturated upstream conditions. In these plots, G_e is calculated at several saturated (temperature, pressure) state points as a function of the vessel quality.

Figure I-9 and Figure I-10 display the variation between the HEM and Henry-Fauske mass fluxes. It can be seen from these figures that discrepancies of 50 percent or more exist for saturated liquid upstream conditions and that significant variations persist for slightly subcooled and low-quality, two-phase stagnation conditions. This disagreement follows from a variation in the assumptions regarding interphase mass transfer. Because the quality is held fixed under the Henry-Fauske model, the discharge is almost entirely in the liquid phase. Under the HEM, however, heat and mass transfer between the phases is allowed and the discharge has a quality that is significantly greater than zero. This discharge possesses a lower density and higher velocity than that predicted by Henry-Fauske. It can be shown numerically that the HEM mass flux prediction will be lower than that of Henry-Fauske for the slightly subcooled, saturated liquid, and low-quality upstream conditions in which the HEM prediction of discharge quality is markedly higher than that of Henry-Fauske.

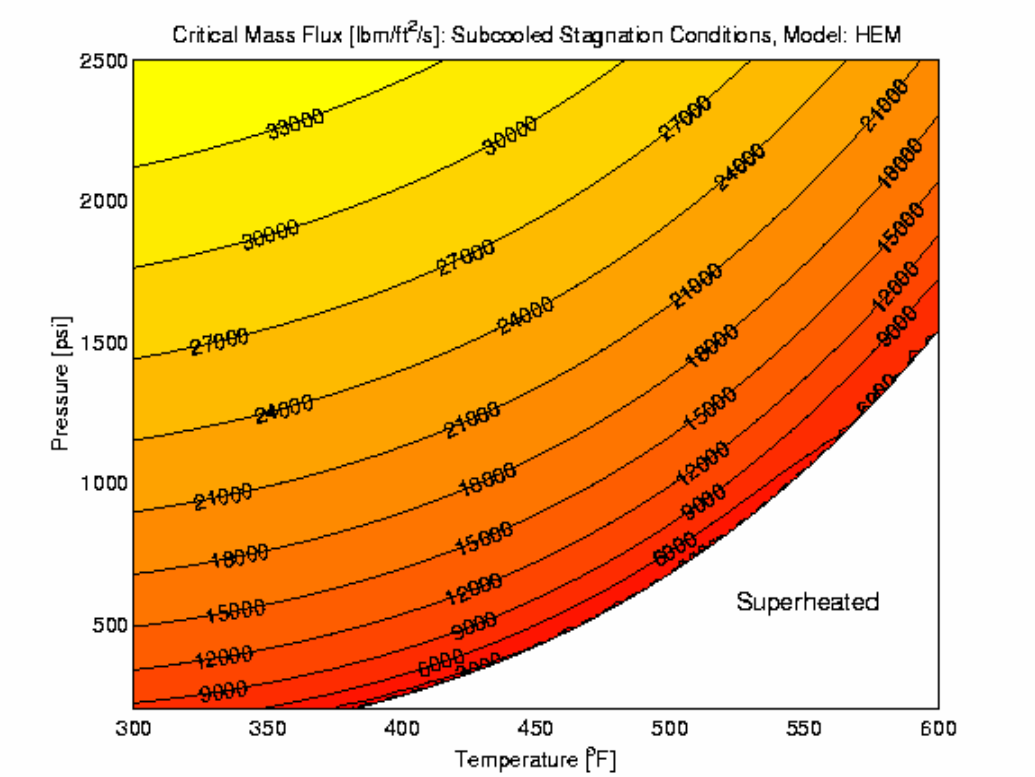

Figure I-5. HEM Critical Mass Flux, Subcooled Stagnation

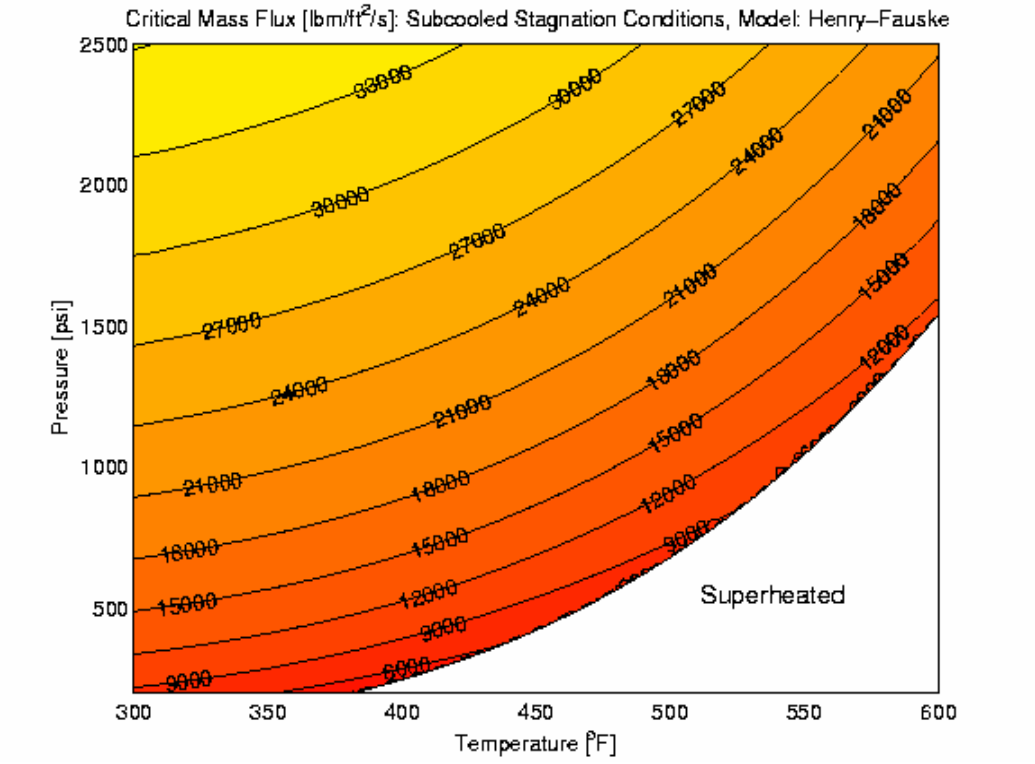

Figure I-6. Henry-Fauske Critical Mass Flux, Subcooled Stagnation

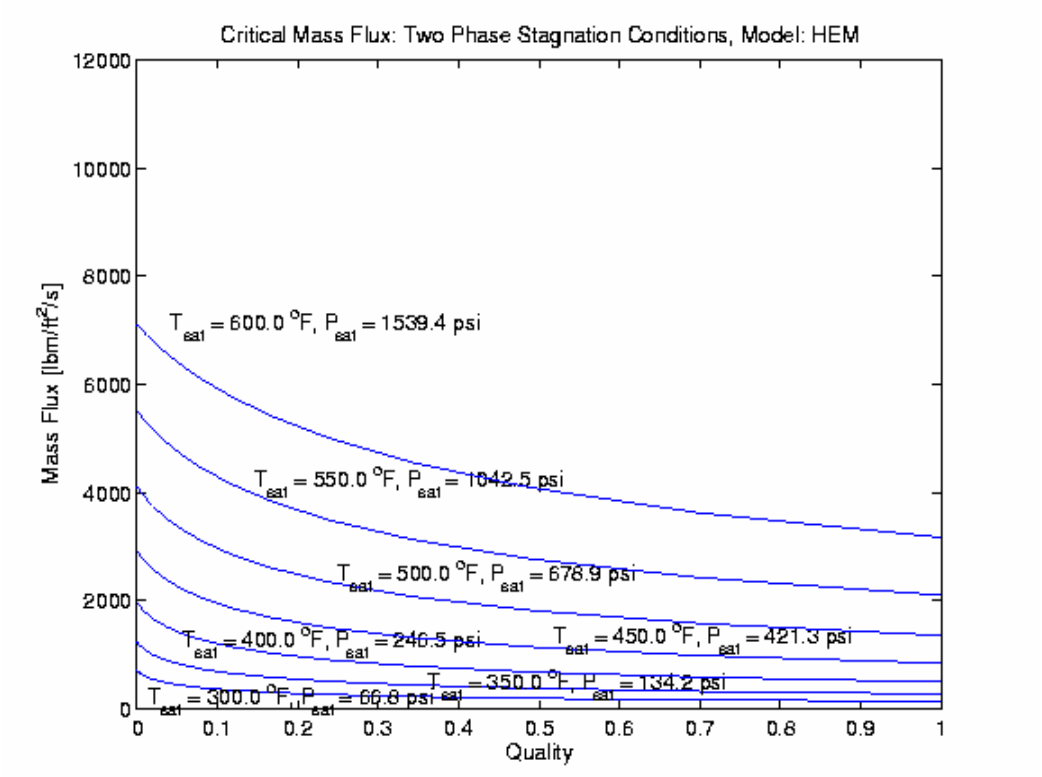

Figure I-7. HEM Critical Mass Flux, Saturated Stagnation

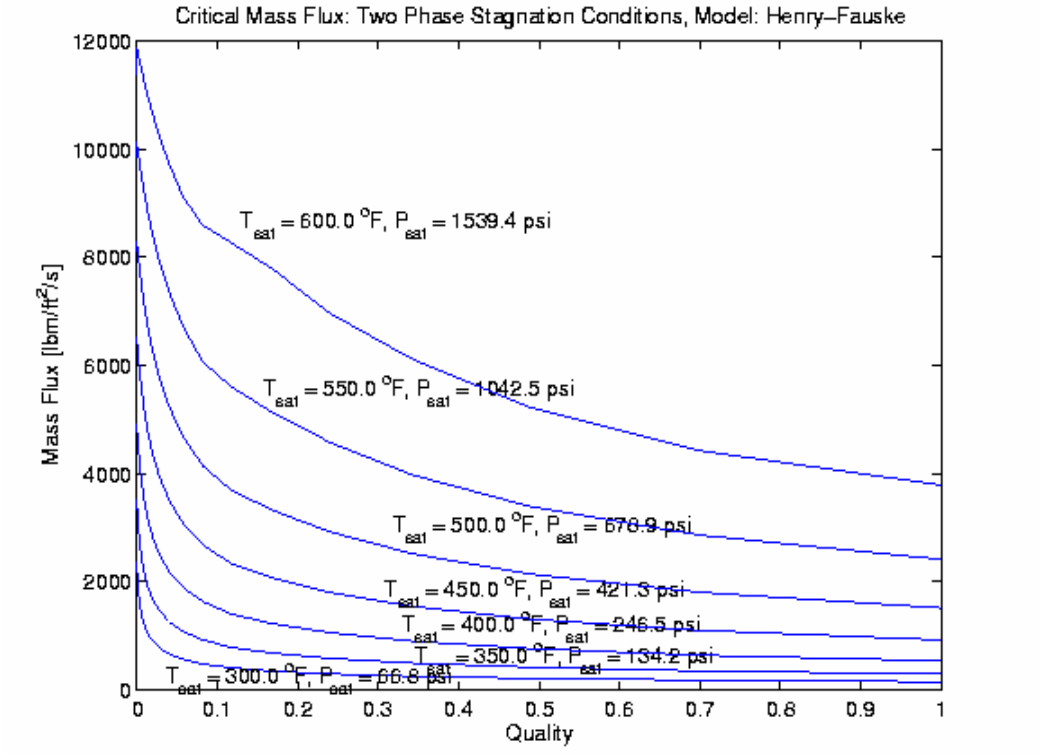

Figure I-8. Henry-Fauske Critical Mass Flux, Saturated Stagnation

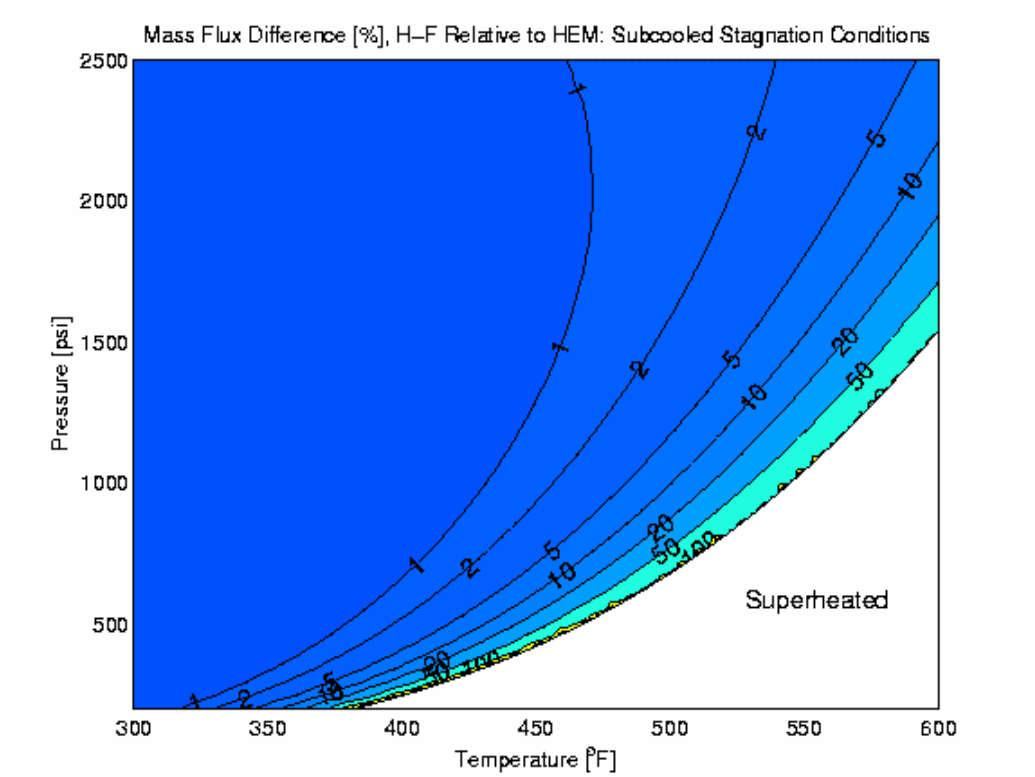

Figure I-9. Mass Flux Difference, Subcooled Stagnation

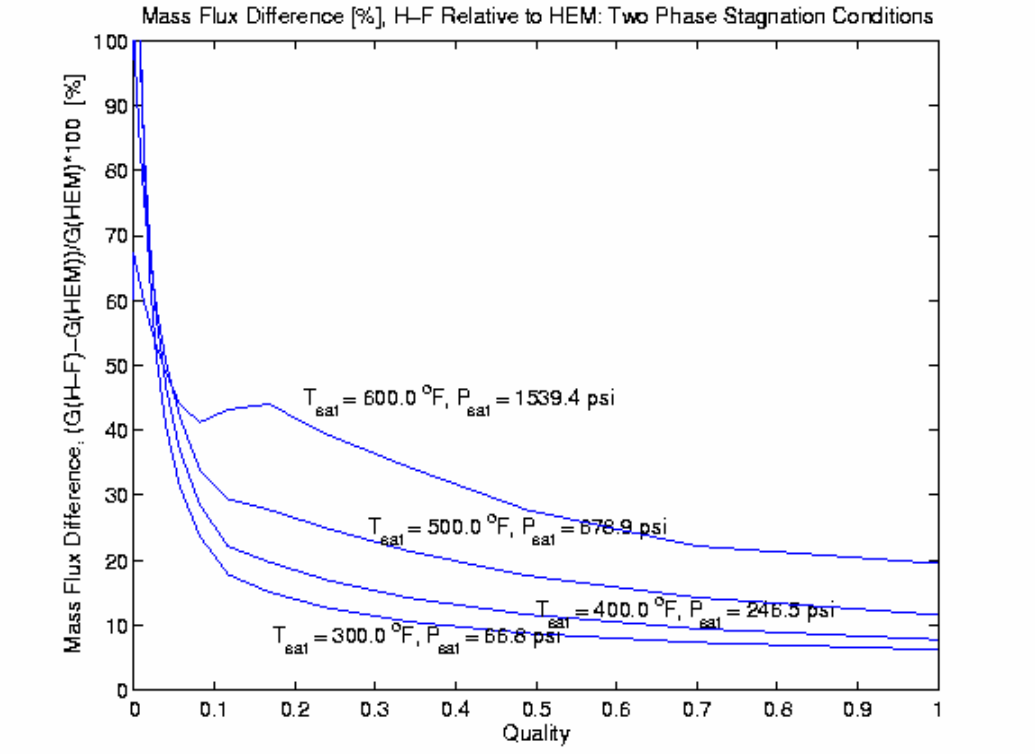

Figure I-10. Mass Flux Difference, Saturated Stagnation

If the advice of the standard is followed, then a significant discontinuity would be observed when the critical flow model transitions from the HEM to Henry-Fauske. The nature and magnitude of this discontinuity is explored further below. Although users of the jet model are in practice unlikely to observe this discontinuity, because during a blowdown, the transition might only occur after significant pressure drops, there is no compelling reason to preserve it. The issue then becomes one of selecting the model that offers the best fidelity to available data. The figures show that the HEM and Henry-Fauske offer comparable predictions for highly subcooled, as well as high-quality two-phase conditions. This is to be expected because under these conditions, both models predict essentially monophasic fluid properties at the throat and the detailed treatment of the interphase heat- and mass-transfer rates offered by Henry-Fauske does not come into play. The benchmarking results reported in HEN71 lead to the conclusion that the Henry-Fauske model exhibits superior agreement to the data under low-quality two-phase and saturated liquid conditions. This alone is sufficient reason to adopt Henry-Fauske; an examination of a second major input to the ANSI jet model, the thrust coefficient, may provide further evidence.

I.5.2 Direct Evaluation of Thrust Coefficients

The thrust coefficient, C_T, acts as a surrogate for the jet thrust force, which the ANSI model does not explicitly call for as an input. This discussion will address only the steady-state thrust coefficient for frictionless, unrestricted flow, but its conclusions can be generalized to include those cases as well. Regardless of upstream conditions, the thrust coefficient is used to correlate the thrust force T, upstream stagnation absolute pressure P_0, ambient pressure P_{amb}, and break area A_e by the expression

$$T = C_T (P_o - P_{amb}) A_e. \tag{I-44}$$

Calculation of the thrust coefficient requires knowledge of local flow conditions at the break. Because these are unknown, unless a critical flow model such as the HEM or Henry-Fauske is used to compute them, pp. 35–45 of the standard provide a series of correlations and figures that may be used as surrogates. Because both Henry-Fauske and the HEM were implemented for the current review, the results obtained from these models will be compared with the recommendations provided in the standard.

The thrust force may be computed by calculating the force that must be exerted to hold in static equilibrium a plate positioned normal to the flow directly at the break point. This thrust is given by

$$T = (P_e - P_{amb}) A_e + \frac{1}{g_c} \rho_e v_e^2 A_e, \tag{I-45}$$

where the static pressure P_e, fluid density ρ_e, and flow velocity v_e are evaluated at the exit. Combining the above equations yields an expression for the thrust coefficient,

$$C_T = \frac{1}{P_0 - P_{amb}} \left(\frac{1}{g_c} \rho_e v_e^2 + \left(P_e - P_{amb} \right) \right). \tag{I-46}$$

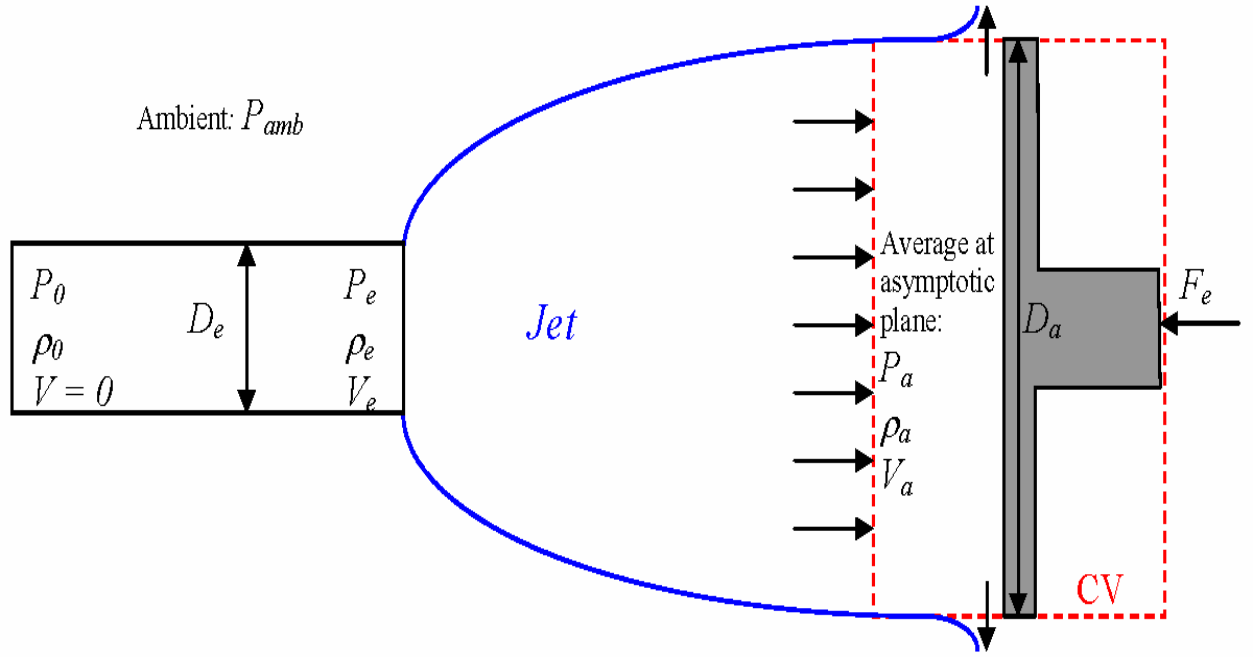

Figure I-4 through Figure I-7 show thrust coefficients computed using pressures and fluid properties evaluated from the HEM and Henry-Fauske models. Regardless of the model, the value of C_T approaches 2.0 for incompressible, highly subcooled liquid and approximately 1.26 for saturated steam. These results agree with theory and are recommended for use in the standard.

For subcooled flashing upstream conditions, p. 42 of the standard recommends use of the curve fits presented by Webb (WEB76). Based on an enthalpy normalization factor

$$h^* = \frac{h_0 - 180}{h_{sat} - 180}, \tag{I-47}$$

where h_0 (Btu/lbm) is the upstream stagnation enthalpy and h_{sat} (Btu/lbm) is the saturated water enthalpy at the stagnation pressure, the correlation is evaluated as

$$C_T = 2.0 - 0.861h^{*2} \text{ for } 0 \le h^* < 0.75 \tag{I-48}$$

and

$$C_T = 3.22 - 3.0h^* + 0.97h^{*2} \text{ for } 0.75 \le h^* \le 1.0. \tag{I-49}$$

For saturated or superheated steam, the standard recommends a thrust coefficient of

$$C_T = 1.26 - P_{amb}/P_0. \tag{I-50}$$

For two-phase steam-water mixtures, the standard provides only a figure that does not address relevant PWR break conditions, and for nonflashing water jets with

temperatures less than the saturation temperature at ambient pressure and pressures greater than ambient, the standard recommends that

$$C_T = \frac{2}{1 + fL/D}, \tag{I-51}$$

where the Fanning friction factor f is normally assumed to be zero for conservatism. The ratio L/D represents a dimensionless flowpath length based on the characteristic length and diameter of the piping between the assumed thermodynamic reservoir and the break location.

Webb claims, and calculations performed for this appendix verify, that his correlations agree with values computed from the Henry-Fauske model to within 3 percent for upstream stagnation pressures ranging from 300 to 2400 psia. The standard does not clearly state this range of applicability. Webb's correlation is recommended when a computational implementation of a critical flow model is unavailable, but two inconsistencies require clarification.

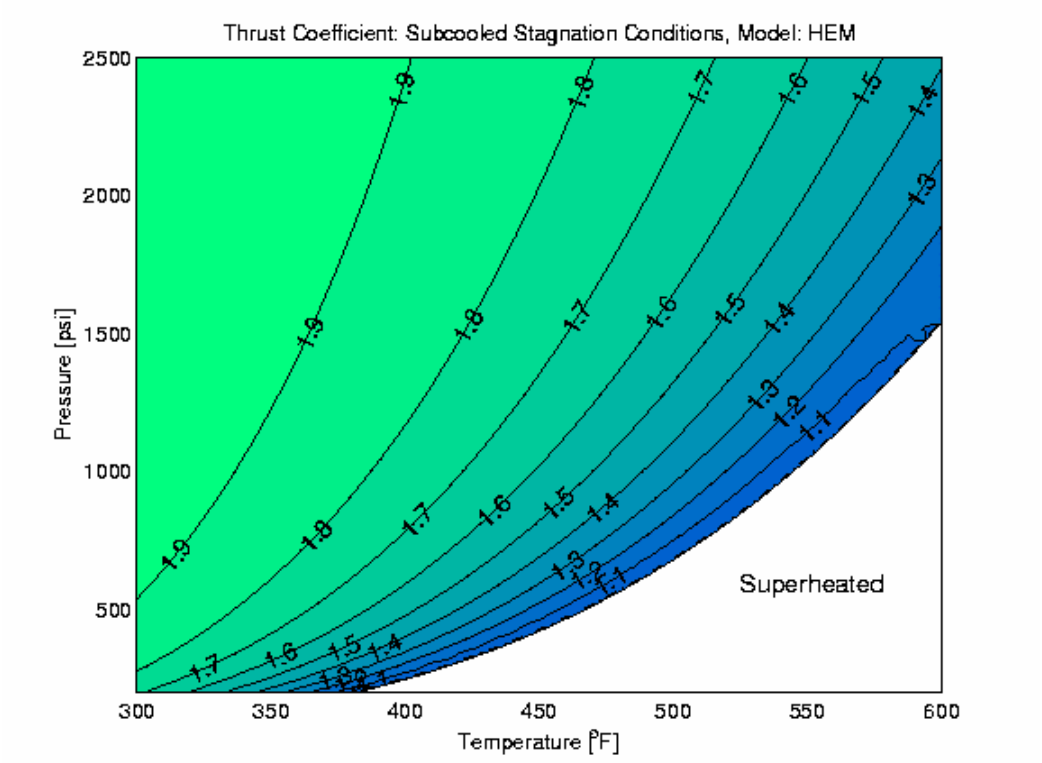

Figure I-11. HEM Thrust Coefficient, Subcooled Stagnation

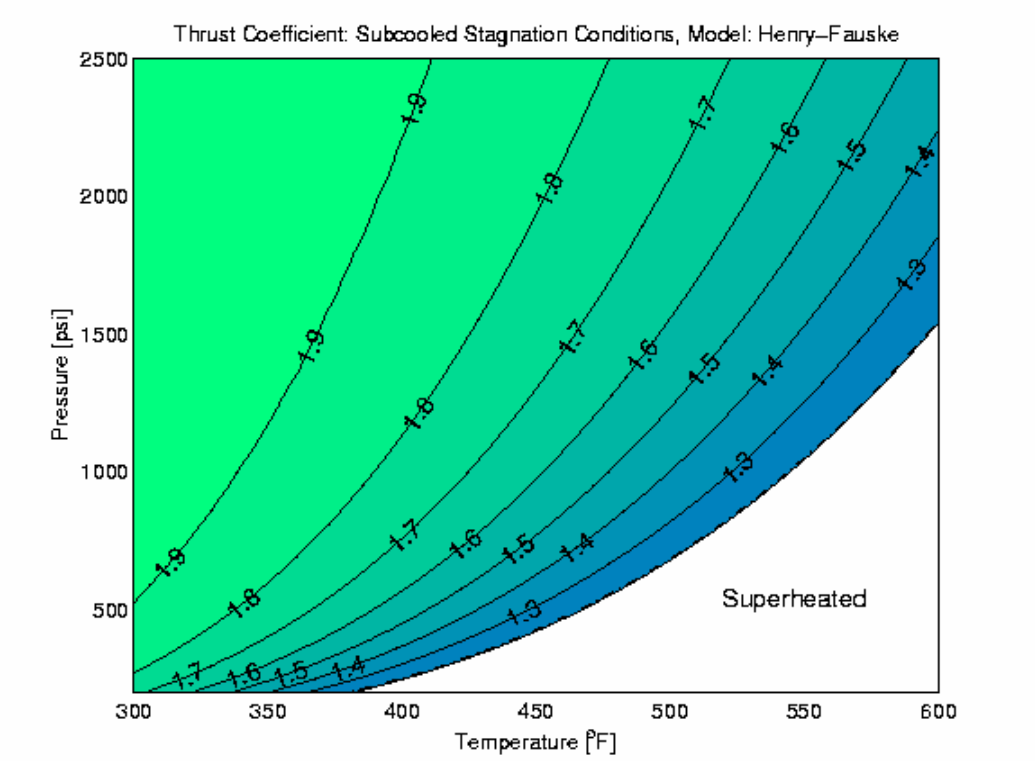

Figure I-12. Henry-Fauske Thrust Coefficient, Subcooled Stagnation

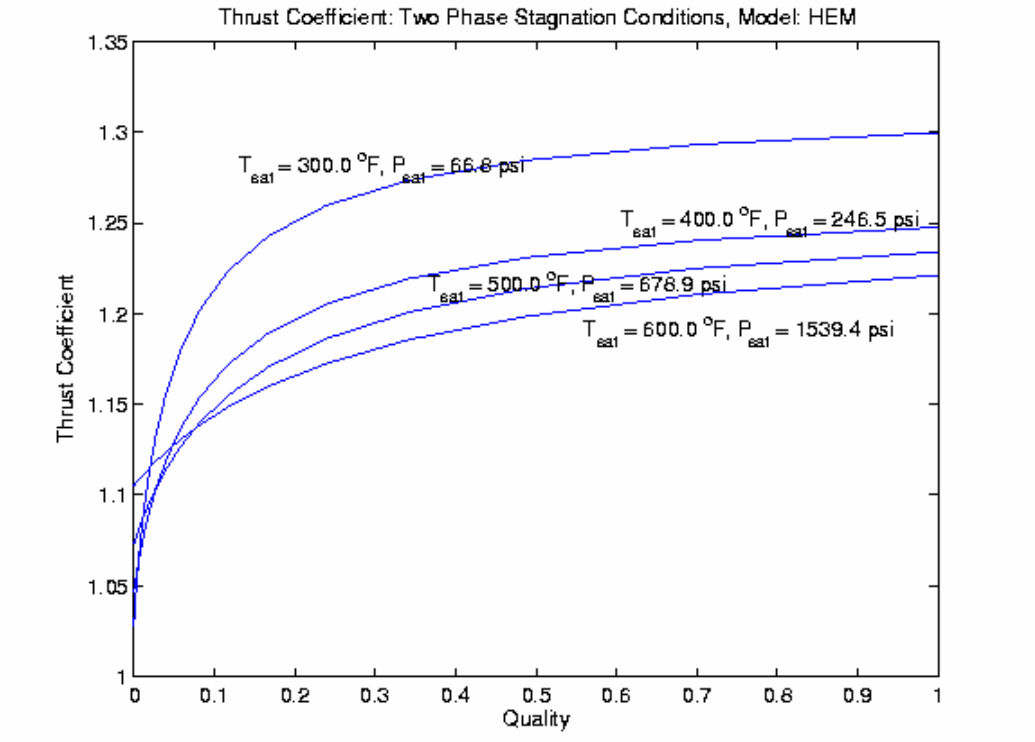

Figure I-13. HEM Thrust Coefficient, Saturated Stagnation

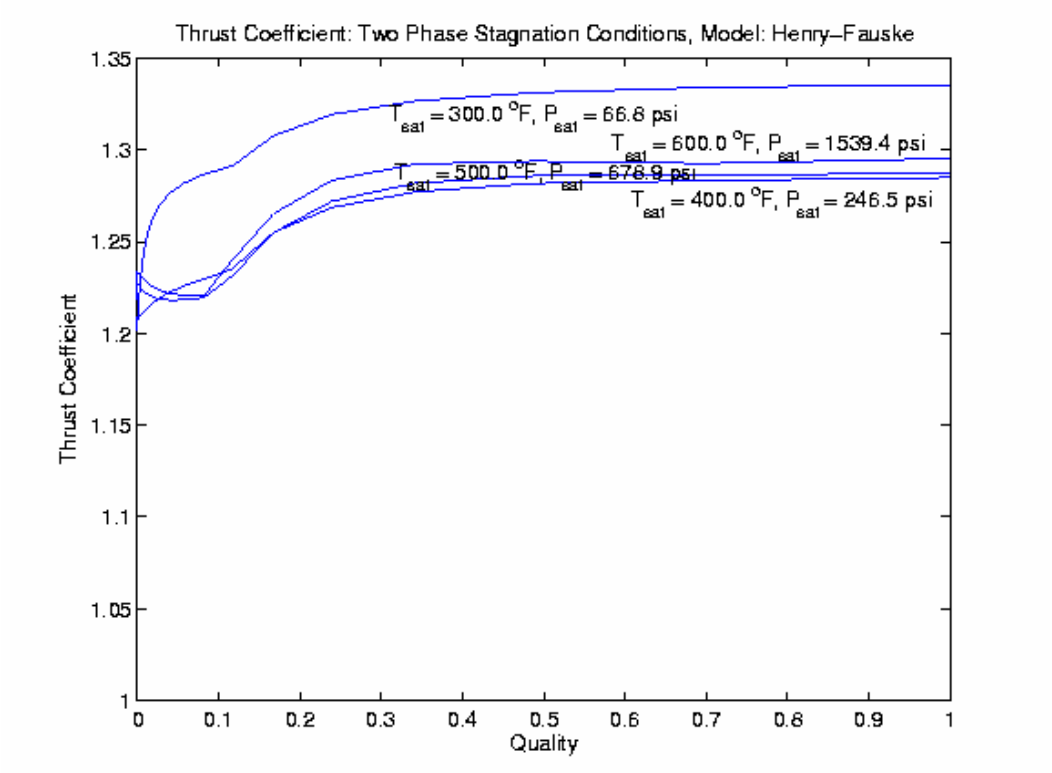

Figure I-14. Henry-Fauske Thrust Coefficient, Saturated Stagnation

In presenting Webb's model, the standard neglects to clarify the "180" figure against which the enthalpy is nondimensionalized. This is, in fact, the enthalpy of saturated water at atmospheric pressure, 14.7 psi. It may be justifiably claimed that during a blowdown, the ambient containment pressure might vary from below atmospheric to significantly above atmospheric. Changes in P_{amb} cannot be accounted for by Webb's model; however, C_T evaluated from the force balance varies weakly with P_{amb}. This effect is not large; even for highly subcooled conditions at the lower end of the range of validity of Webb's correlation, $P_0 = 300$ psia, neglecting P_{amb} altogether changes the thrust coefficient evaluated from the force balance by less than 5 percent.

The standard also places insufficient emphasis on the fact that Webb's correlation is obtained from calculations using the Henry-Fauske model. Because this is the case, employing HEM-derived mass fluxes with thrust coefficients obtained from this correlation propagates a significant inconsistency. Figure I-8 shows that significant deviation exists between thrust coefficients computed from the outlet conditions provided by the two critical flow models. The use of Henry-Fauske-derived thrust coefficients with HEM mass fluxes will result in overprediction of damage radii. This follows because the larger Henry-Fauske thrust coefficient implicitly imposes a higher flow density, velocity, and/or static pressure at the break plane.

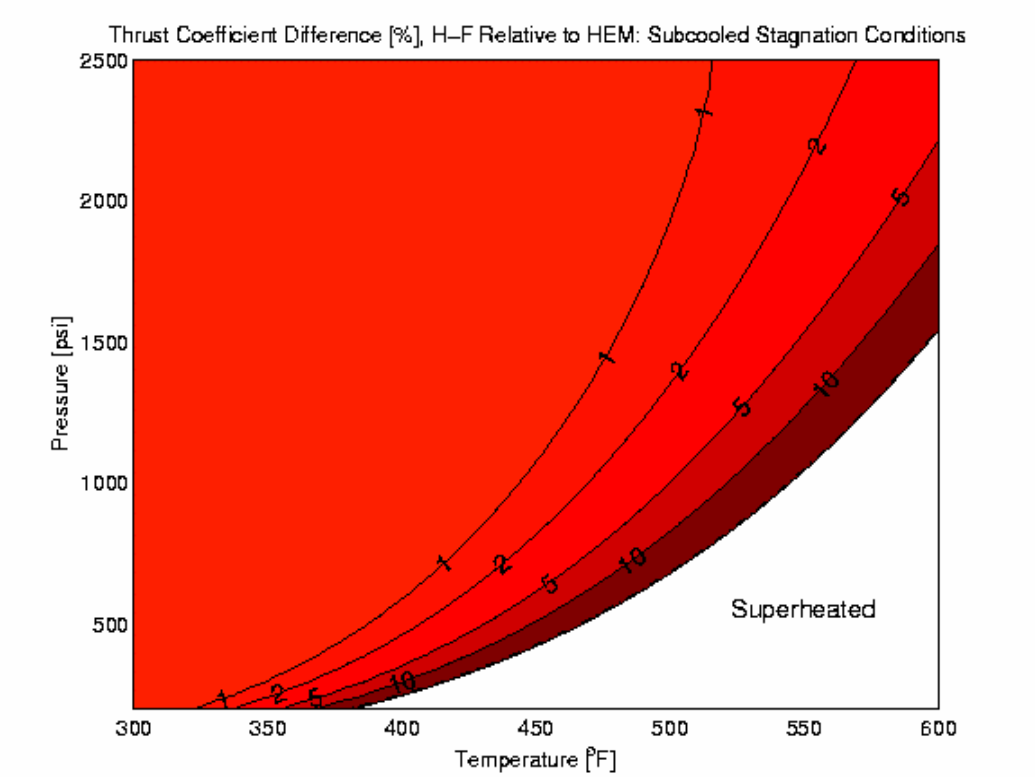

Figure I-15. Thrust Coefficient Difference, Subcooled Stagnation

I.5.3 Effects of Flow Models on Jet Behavior

While the sensitivity of the jet pressure contour map in its entirety to variations in C_T is too complicated to permit analytic treatment, the effect of variation of C_T on conditions at the asymptotic plane can be used for illustration. Equation (I-43) shows that the jet area A_a at the asymptotic plane is inversely proportional to C_T. However, from conservation of mass, equation (I-40), the average flow velocity at the asymptotic plane v_a is inversely proportional to A_a and, thus, directly proportional to C_T. This conclusion can be drawn because the average fluid density, ρ_a, at the asymptotic plane depends, in the ANSI formulation, only upon upstream stagnation conditions. The dynamic pressure of the fluid, which is proportional to the square of its velocity, thus varies as C_T^2. The results of decreased jet cross-sectional area and increased velocity from the larger Henry-Fauske thrust coefficient will be a narrower, more penetrating jet and larger volume-equivalent radii at a given damage pressure.

In fact, it can be seen from Figure I-16 that the thrust coefficient for upstream conditions at or near saturation as derived from the HEM is significantly lower than the value of 1.26 recommended in Figure B-5 of the standard. The inconsistency inherent in use of the 1.26 value with the HEM mass flux would again result in overprediction of volume-equivalent radii. This additional consideration strengthens the recommendation that the Henry-Fauske method be employed for all flow regimes when performing the calculations outlined in the standard.

As mentioned above, the critical mass flux G_e derived from the HEM will be smaller, significantly so for stagnation conditions lying near the liquid saturation line in (P, h) space, than that obtained from Henry-Fauske. Because this is the case, it is also useful to address the behavior at the asymptotic plane when G_e is varied, with C_T held constant. Following the same reasoning pursued above when the thrust coefficient was varied, the jet area at the asymptotic plane varies as G_e^2. The average jet velocity at that location, v_a, on the other hand, behaves as $v_a = k G_e / A_a$ so that $v_a \sim 1/G_e$. Thus, a seemingly paradoxical conclusion is reached, namely that reducing the mass flux while holding the thrust coefficient constant increases the velocity at the asymptotic plane and might *increase* the volume-equivalent radii.

Although this thought experiment is not conclusive or comprehensive—the location of the asymptotic plane, for instance, also depends on G_e and C_T and has not been taken into account—numerical computations verify its conclusions. Table I-1 shows critical flow model results for five of the upstream conditions given in Table I-2. The conditions selected from that table are #8, PWR Hot-Leg Initial; #1, PWR Cold-Leg Initial; #2, PWR Cold-Leg Blowdown; #9, BWR Hot Leg; and #11, Main Steamline. All three PWR stagnation states are subcooled; the BWR state is two phase with a quality of 0.15 and the steamline case is superheated by 35 °F. In addition to the mass flux, G_e, thrust coefficient, C_T, and discharge velocity, v_e, obtained, the table also shows the volume-equivalent damage radii for the 10 and 150 psig contours. It might be intuitively expected that the Henry-Fauske model is the more conservative when calculating damage radii because it predicts critical mass fluxes and thrust coefficients that are greater than those of the HEM, but, as shown in the table, particularly for initial conditions nearing saturation, this is not the case.

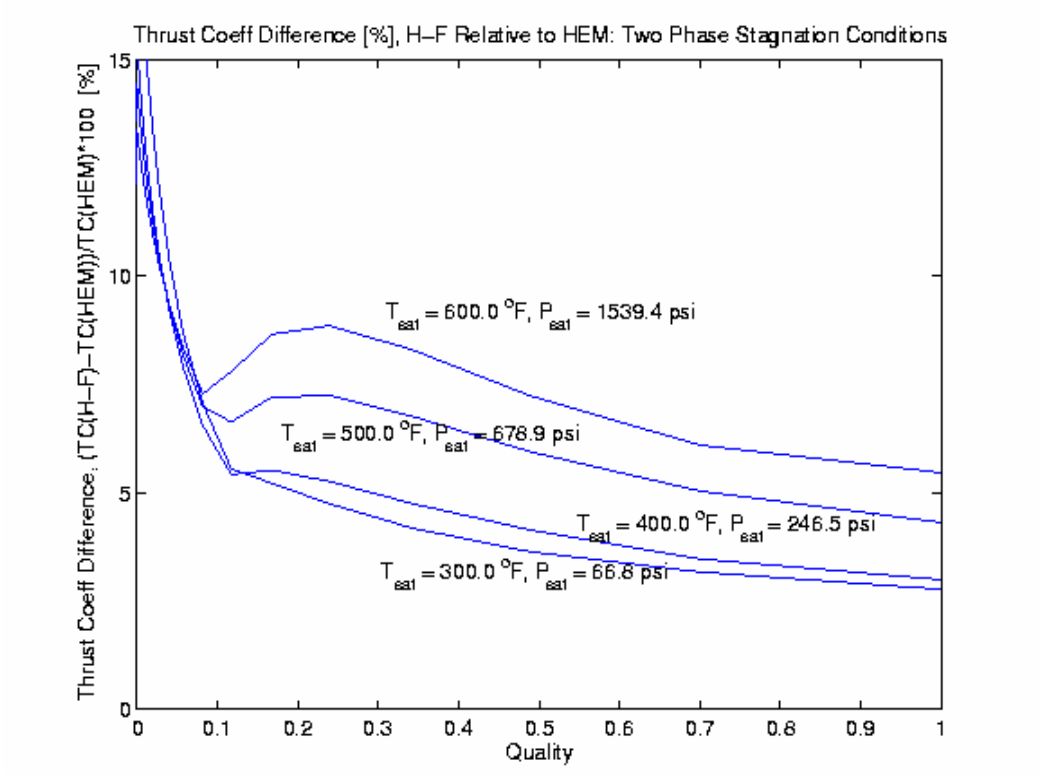

Figure I-16. Thrust Coefficient Difference, Saturated Stagnation

Table I-1. Critical Flow Model Results and Their Effect on Volume-Equivalent Damage Radii

	Critical Mass Flux G_e (lbm/ft^2/s)		Thrust Coefficient C_T (--)			Breakflow Velocity v_e (ft/s)		150-psig* Damage-Pressure Radius (pipe diameters)		10-psig* Damage-Pressure Radius (pipe diameters)	
	HEM	**H-F**	**HEM**	**H-F**	**Webb****	**HEM**	**H-F**	**HEM**	**H-F**	**HEM**	**H-F**
1. Cold-Leg Initial (2250 psia, 530 °F)	**24850**	**25330**	**1.62**	**1.64**	**1.63**	**522**	**527**	**1.48**	**1.48**	**12.00**	**12.04**
2. Cold-Leg Blowdown (393 psia, 291 °F)	**13370**	**13390**	**1.88**	**1.89**	**1.90**	**232**	**232**	**0.96**	**0.96**	**4.42**	**4.43**
8. Hot-Leg Initial (2250 psia, 630 °F)	**11840**	**15400**	**1.17**	**1.28**	**1.28**	**296**	**382**	**1.60**	**1.59**	**11.14**	**11.07**
9. BWR Hot Leg (1040 psia, 550 °F, X = 0.15)	**3920**	**5260**	**1.16**	**1.26**	**N/A**	**178**	**158**	**1.11**	**1.12**	**7.81**	**7.80**
11. Main Steamline (910 psia, 570 °F)	**1800**	**N/A**	**1.24**	**N/A**	**N/A**	**464**	**N/A**	**1.08**	**N/A**	**7.58**	**N/A**

* Damage-pressure radii are given as multiples of the break diameter. They are obtained by constructing spheres with volume equal to the volume enclosed by a given jet stagnation pressure contour. See Section I.3 for further elaboration.

** Shown for purposes of comparison only; not used in damage-pressure-radius calculations given in this table.

I.6 Sample Calculations

A MATLAB routine called ANSIJet (see Attachment 1 ADAMS document ML042640274) implemented the ANSI model presented in the previous sections for predicting stagnation pressures in an expanding jet. This programming language was selected for convenient interface with steam-table routines available from NIST. Several cases relevant to both PWR initial break and blowdown conditions were evaluated. Two generic BWR state points were also evaluated, as were three cases applicable to steamline flow in secondary loops. Two of these relate to a single-pass Babcock & Wilcox steam generator discharging superheated (by ca. 35°F) steam; the third applies to a Combustion Engineering U-tube heat exchanger and is assumed to yield saturated steam. Table I-2 defines these conditions for later reference by case number. Note that Figure I-1 corresponds to the cold-leg initial break condition defined as Case #1.

Table I-2. Comparative Calculation Set Using ANSI Jet Model

Case #	Description	System Stagnation Conditions		
		P_0 (psia)	T_0 (°F)	Quality
1	cold-leg initial[1]	2250	530	Subcooled
2	cold-leg blowdown[1]	393	291	Subcooled
3	cold-leg blowdown[1]	857	351	Subcooled
4	cold-leg blowdown[1]	1321	411	Subcooled
5	cold-leg blowdown[1]	1786	471	Subcooled
6	10% greater pressure than Case 1	2475	530	Subcooled
7	cold-leg initial[2]	2250	540	Subcooled
8	hot-leg initial[3]	2250	630	Subcooled
9	BWR hot leg[4]	1040	550	0.15
10	BWR cold leg[4]	1040	420	Subcooled
11	main steamline (MSL)—Babcock & Wilcox (B&W)[4]—full power	910	570	Superheated
12	B&W MSL—design conditions[4]	1075	603	Superheated
13	MSL—Combustion Engr. Calvert Cliffs[5]	846	525	1.0

[1] From RAO0
[2] From NEI04
[3] From DUD76
[4] From RAH92
[5] From LOB90

Jet-pressure isobars for Cases 1 through 6 were integrated over a wide range of values and converted to equivalent spherical diameters. Figure I-17 presents these results. Recall that the ANSI-model stagnation pressure is used as a correlation parameter that corresponds to observed damage in debris generation tests. The Figure I-17 abscissa is labeled as “Damage Pressure” because of the use of this correlation. Case 1 represents

a previously studied hydraulic condition (RAO02) that will be used as the reference case. Reading from the figure, a damage pressure of 10 psig corresponds to an equivalent jet radius of approximately 12 pipe diameters. Note that equivalent radii climb sharply for damage pressures below 20 psig.

This set of calculations suggests that the state-point pressure of the jet dominates the determination of isobar volumes. Case 1 bounded other cases that are not shown in Figure I-17. Case 7, the nominal PWR cold-leg condition recommended in the GR, was almost indistinguishable from Case 1. The reference case also bounded Case 8, a nominal hot-leg break condition, except at damage pressures greater than 120 psig. Hot-leg conditions are much closer to saturation (630°F vs. 653°F); therefore, the shapes of the pressure contours change near the core. Case 6 was run as a perturbation check for plants that may at times have higher operating pressures than the nominal value of 2250 psig. Although the pressure increase was 10 percent higher than the reference, the maximum deviation in spherical volume was only 8 percent; therefore, a linear adjustment for higher pressure would be conservative in the absence of a full jet-model analysis.

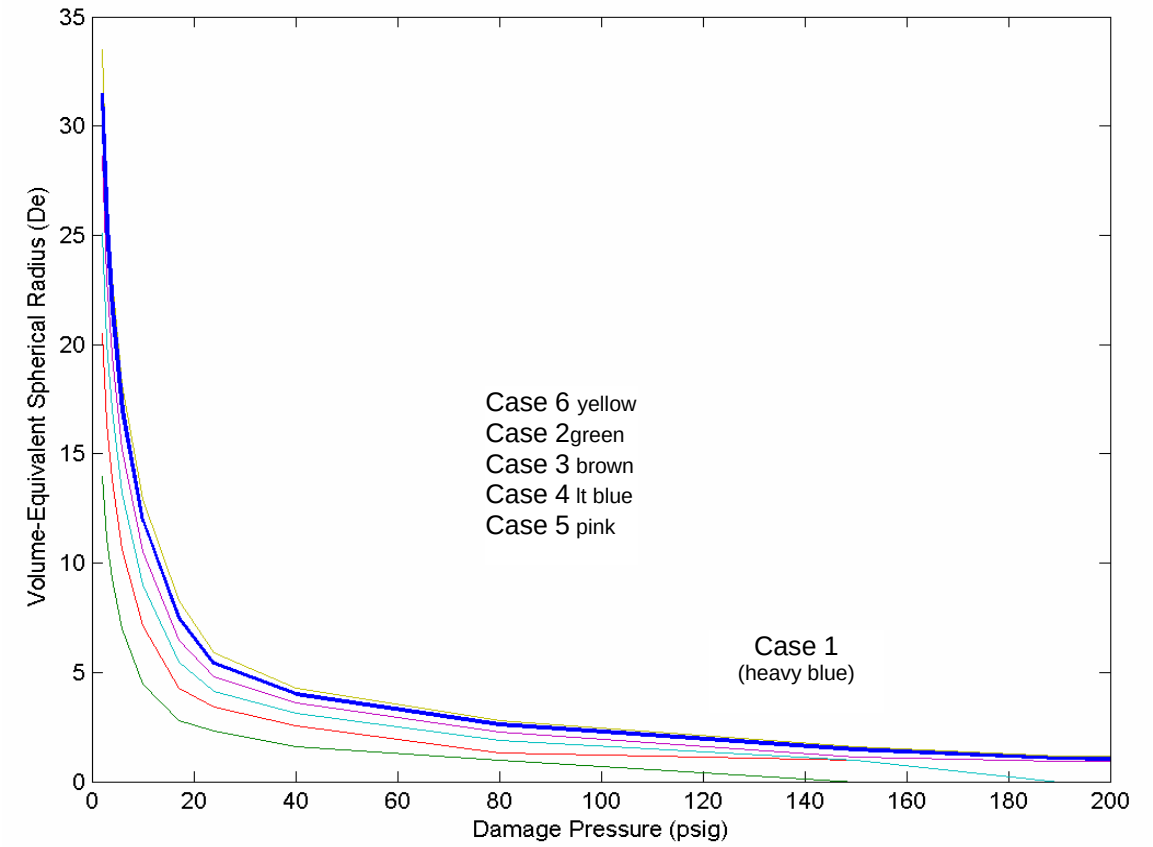

Figure I-17. Comparison of ANSI Jet-Model Equivalent Spherical Radii for Six Initial Break Conditions

Figure I-18 depicts the damage radii associated with the BWR hot-leg and cold-leg conditions of Cases 9 and 10. Given the lower stagnation pressures pertinent to BWR coolant, the equivalent radii are, as expected, smaller than was the case for PWR

conditions at comparable values of damage pressure. Figure I-19 provides the radii obtained for the three steamline cases. Two of these, Cases 11 and 13, represent full-power operating conditions. The third, Case 12, is a design specification included to serve as a conservative bounding scenario. Given that the thrust coefficient is nearly invariant at a value near 1.26 for high-quality two-phase and superheated upstream conditions, it appears reasonable to expect damage radii in such regimes to respond linearly to variation in the stagnation pressure. Figure I-20 provides a pressure contour plot for the steamline break condition. This figure compares to Figure I-1 for PWR cold-leg stagnation conditions. One of the subtle differences between these figures is the higher centerline pressure exhibited by the MSL case to axial distances of about 30 pipe diameters. The steamflow exhibits a narrower jet that is higher velocity at the centerline, leading to a greater dynamic contribution to the stagnation pressure. Differences in the initial pressure should also be considered when visually comparing Figure I-1 and Figure I-20.

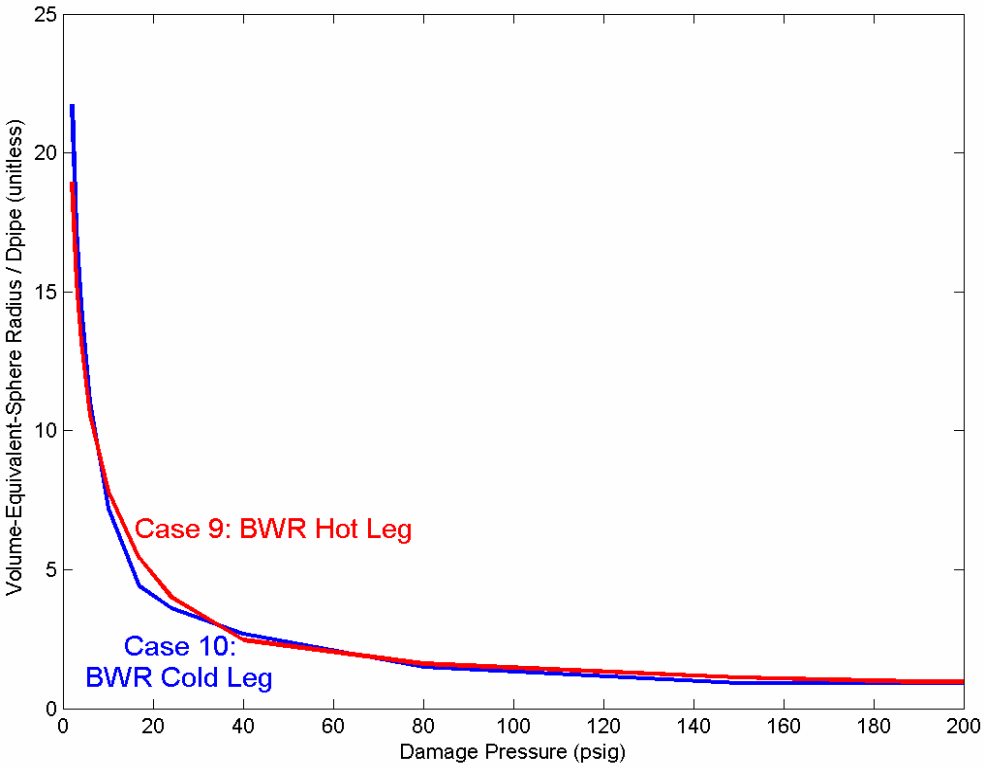

Figure I-18. Comparison of ANSI Jet-Model Equivalent Spherical Radii for BWR Break Conditions

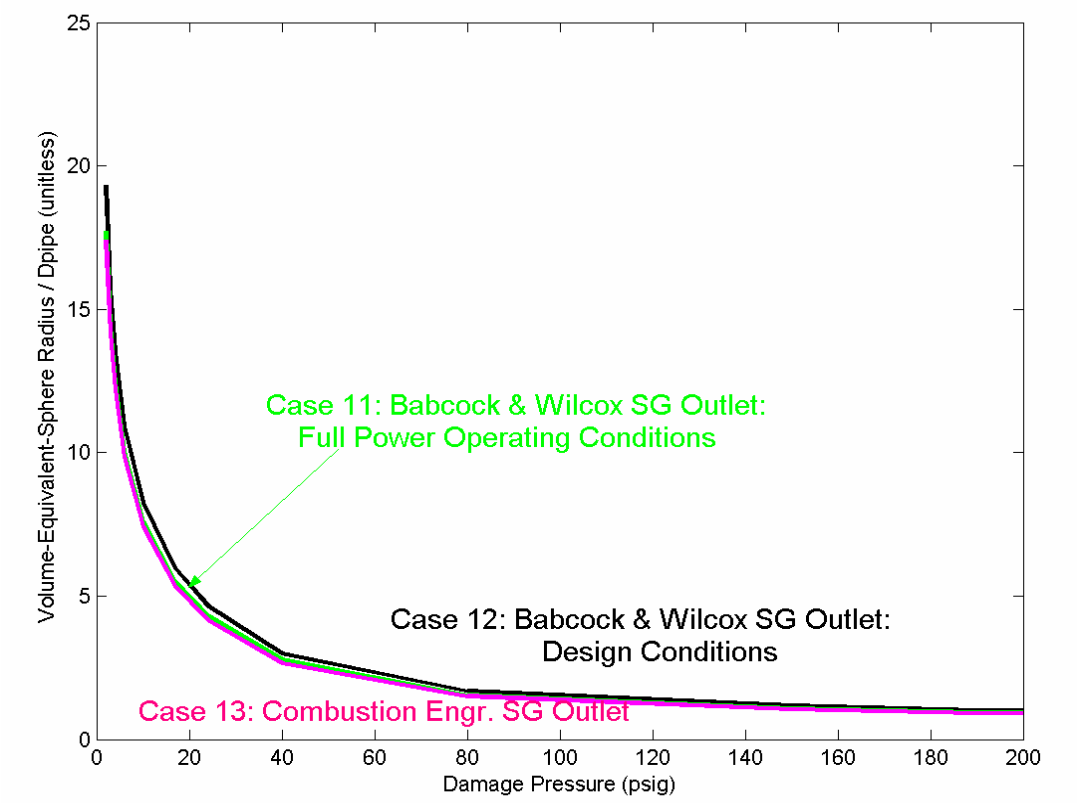

Figure I-19. Comparison of ANSI Jet-Model Equivalent Spherical Radii for MSL Break Conditions

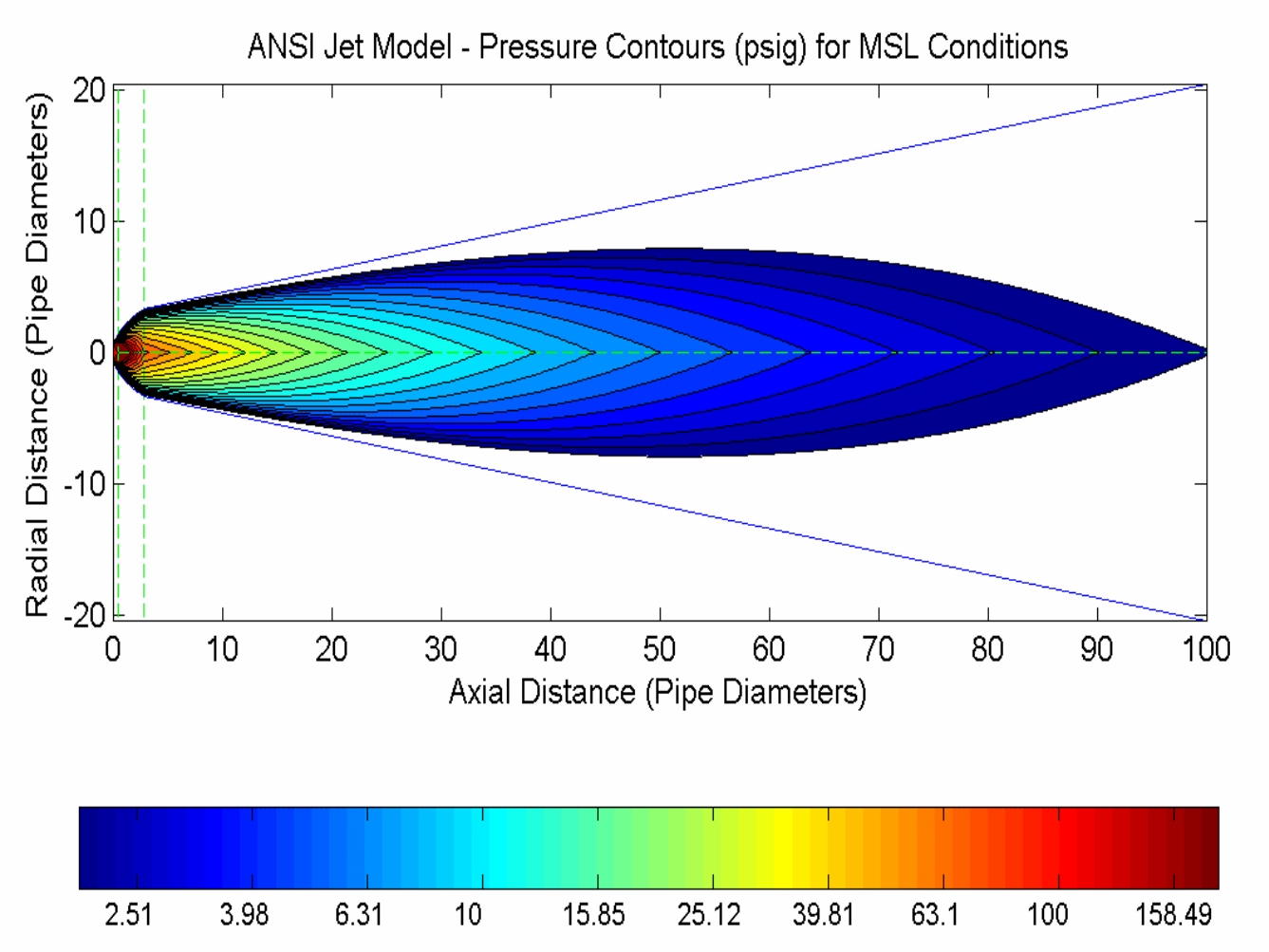

Figure I-20. ANSI Jet-Model Stagnation Pressures for MSL Break Conditions (570°F, 910 psia)

Other useful information can be extracted from the jet model in addition to equivalent spherical diameters derived from spatial volume integrals. Appendix D to the ANSI standard suggests estimating target temperatures by evaluating a thermodynamic state point using the jet pressures P_j and the initial enthalpy h_0. Presuming that the model supplies realistic, nonisentropic impingement pressures (at least in the longitudinal direction), this approach will give the temperature of the stationary fluid striking the surface of a large target. Actual target temperatures might vary with internal heat conduction properties and external drag coefficients that affect aerodynamic heating, but it is instructive to compute this approximation nonetheless. Figure I-21 illustrates the isotherm plot corresponding to Case 1 for the reference cold-leg break.

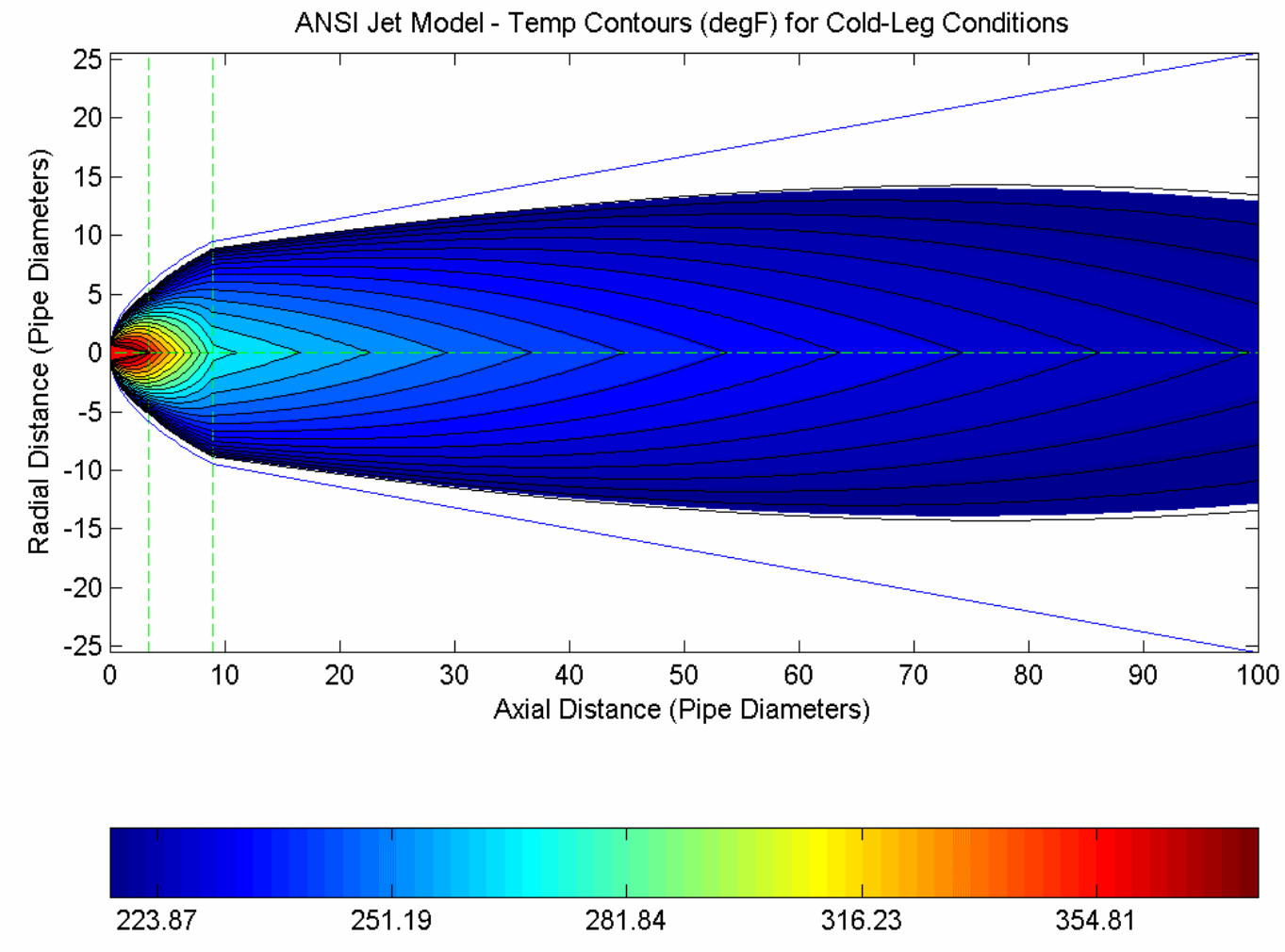

Figure I-21. Isotherm Contours for the Reference Cold-Leg Break at 2250 psia and 530°F

The somewhat surprising attribute of the isotherm map is how slowly the impingement temperature changes beyond the range of 10 to 15 pipe diameters downstream of the break. For potential debris-generation mechanisms that are suspected to have important thermal responses, this information can directly benefit both the specification of relevant test parameters and the interpretation of existing test data. For example, a test performed at 280°F that exhibits good damage resistance demonstrates substantially less spatial vulnerability to high-temperature jets than a test performed at 220°F. As with pressure contours, isotherm volumes can also be mapped to equivalent spherical volumes, and because the ANSI model exhibits spatial monotonicity (uniformly increasing or decreasing in every direction) in all physical jet properties, there is a unique correspondence between pressure, temperature, and contour volume.

Another impingement-state parameter of interest is the fluid quality. There has been a long-standing debate regarding the potential for enhanced debris generation in the presence of entrained water droplets compared with that observed for high-quality steam and for air-jet surrogates. While the ANSI model cannot answer this concern, it may

offer information on the spatial extent of the phenomena. Subject to the same interpretations and approximations as those discussed for impingement temperature, the jet quality can also be evaluated at P_0 and h_0. Figure I-22 illustrates contours of equal two-phase steam quality for the reference cold-leg break. Similar to temperature, the fluid quality changes slowly beyond a range of 10 to 15 pipe diameters and maintains a nominal value between 0.25 and 0.35. This range would be considered low-quality steam for turbine generator applications and might be viewed with concern for its potential erosion effects on stainless steel rotor blades. Certainly, the time regimes of jet impact and in-service steam components are drastically different, but the potential damage mechanisms are the same.

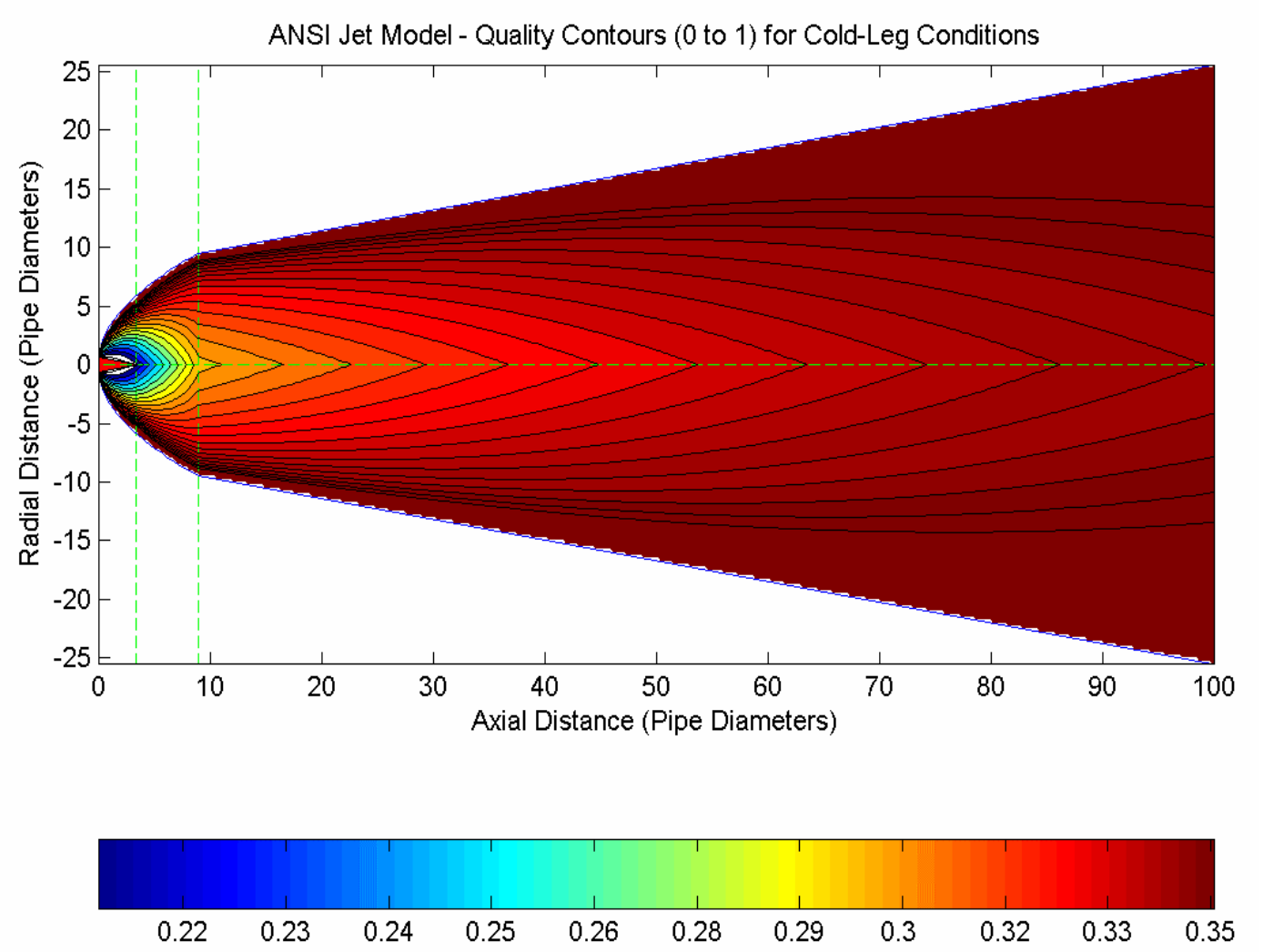

Figure I-22. Contours of Equivalent Steam Quality for the Reference Cold-Leg Break at 2250 psia and 530°F

The thermodynamic treatment of two-phase saturated conditions in the ANSI standard is inherently a homogeneous mass-mixture model. That is, the two-phase mixture is considered to be a single fluid with equivalent mass-weighted thermodynamic properties.

This assumption, along with that of equal phase velocities in the jet, is justified by Lahey and Moody (LAH84). Therefore, void fractions could be estimated from the local pressures and qualities. Under this assumption, it was found that the qualities shown in Figure I-19 would correspond to void fractions greater than 0.95 for all regions of the jet apart from the core. While Figure I-19 could be separated into the fluid and vapor mass fractions using the saturation properties and the definition of quality, the real issue of momentum transfer to a target could not be addressed with convincing accuracy. Theoretical treatments of two-phase transport introduce concepts of condensate nucleation, interphase velocities, droplet drag coefficients, and void fraction (space between droplets) that are difficult to measure experimentally. Pursuing this analysis with the present ANSI model would exceed the scope of its purpose and fidelity.

In summary, Table I-3 presents a set of concomitant values for pressure, temperature, quality, and equivalent spherical radius that characterize the approximate impingement conditions in an expanding jet generated by a cold-leg break at 2250 psia and 530°F. With respect to equivalent spherical diameter, this reference case is observed to bound all break conditions of interest for a PWR accident analysis. Table I-4 lists intermediate parameter values computed by ANSIJet for the reference break conditions. This information may be useful for comparisons of independent implementations of the jet model.

Table I-3. Summary of Jet Properties for the Reference Cold-Leg Break

P_{jet} (psig)	T_{jet} (°F)	Q_{jet}	R_{sphere}
2	218.7	0.35	31.5
3	221.8	0.34	25.4
4	224.6	0.34	21.6
6	230.0	0.34	17.0
10	239.6	0.33	11.9
17	253.7	0.32	7.5
24	265.5	0.31	5.4
40	287.0	0.29	4.0
80	324.2	0.26	2.6
150	366.1	0.21	1.5
190	384.0	0.20	1.1
2250	530.0	0.00	0.9

Table I-4. Intermediate Parameters Computed by the ANSI Jet Routine for the Reference Cold-Leg Break Conditions

Vessel Pressure	P_0	[psia]	2250
Vessel Temp	T_0	[deg F]	530
Vessel Quality	X_0	[-]	-0.430084
Vessel Density	r_0	[lbm/ft^3]	48.0879
Vessel Enthalpy	h_0	[Btu/lbm]	522.455
Sat Temp at P_0	T_{sat}	[deg F]	653.014
Liq Sat Enth at P_0	h_f	[Btu/lbm]	700.946
Vap Sat Enth at P_0	h_g	[Btu/lbm]	1115.96
Ambient Pressure	P_{amb}	[psia]	14.7
Pres at Asym Plane	P_a	[psia]	14.7
Dens at P_a, h_0	rma	[lbm/ft^3]	0.105653
Computed Thrust Coeff	TC	[-]	1.64413
Crit Mass Flux	G_e	[lbm/ft^2/s]	25329.2
T_{sat} at P_{amb}	T_{satamb}	[deg F]	212.238
Liq Sat Enth at P_{amb}	h_{famb}	[Btu/lbm]	180.176
Vap Sat Enth at P_{amb}	h_{gamb}	[Btu/lbm]	1150.28
Degrees Subcooling	$delT_{sub}$	[deg F]	123.014

I.7 Comparison of ANSI Model to Empirical Model of Kastner

Kastner et al. (KAS88) has generated a substantial body of experimental jet force and pressure distribution data. This work was carried out for upstream pressures ranging from 5 to 100 bar, temperatures from 20 to 310°C, and orifice diameters from 1 to 6.5 cm. A large plate was positioned at locations downstream of the orifice; the location of this plate along the jet axis was varied from 0.25 to 10 orifice diameters. Impingement pressures were recovered through a series of pressure taps located upon the plate. From this data, Kastner prepared empirical models for jet behavior given subcooled and saturated upstream stagnation conditions. Because the Kastner model has been formulated through regression analyses upon the data, it offers a convenient avenue for comparison of the ANSI model to experiment-based results.

Kastner's reference presented only the subcooled stagnation model in usable form. Therefore, two state points that fall within the range of validity of this model are selected for this comparative assessment. These are both relevant to BWR conditions—Case 10 from Table I-2 (420°F, 1044 psi) and a less-subcooled condition at the same pressure (516°F, 1044 psi). The quantities to be compared are jet centerline pressure, recovered jet thrust force, and radial pressure distribution. Given the conditions for which Kastner's model was derived, the comparison can only be considered valid for axial distances of less than 10 orifice diameters.

Figure I-23 compares the jet centerline pressure predicted by each model. The discontinuity predicted by the ANSI model when transitioning from the core to the freely expanding region where a high-quality, two-phase mixture flashes off of the core is clearly evident. Kastner's correlations, although they do include the core region, do not

preserve this feature. Agreement for the more highly-subcooled upstream condition is poor, with the higher pressure predicted by Kastner implying that, near the jet centerline, a monophasic liquid region might persist farther downstream of the break location.

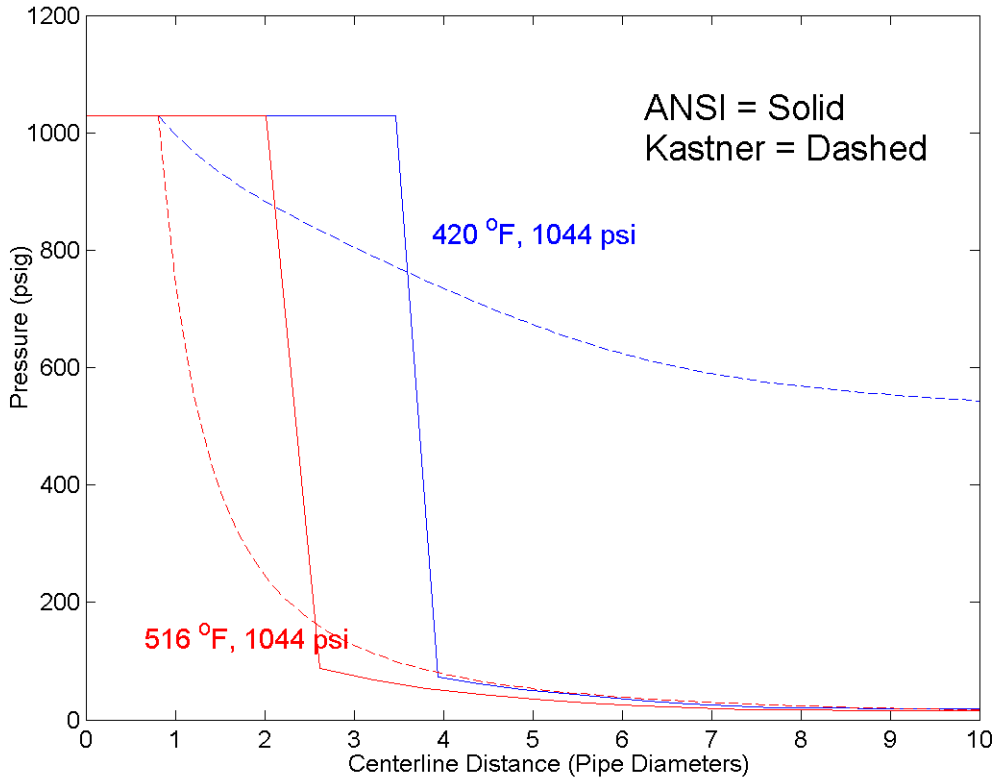

Figure I-23. Comparison of Jet Centerline Pressure Predictions

The radial pressure distributions adopted by the two models present strongly divergent functional forms. Under the ANSI model, the distribution takes on a triangular form. Hence the pressure behaves as an almost-linear function of radial position (exactly linear in Jet Region III of the standard), taking on its maximum value at the centerline and going to zero at the jet boundary. (See Section I.3.2 for further discussion.) Kastner observed that a Gaussian distribution closely approximates the radial impingement pressure. For a given subcooled upstream stagnation condition, Kastner's fit to the data results in a Gaussian radial pressure profile with a half-width independent of axial (downstream) position.

The ANSI model also preserves the concept of an asymptotic plane from classical jet theory as presented in LAH84. Recall that this plane is located at the downstream location at which the jet static gauge pressure is assumed to vanish. Under the ANSI model, downstream of the asymptotic plane mixing with the environment is assumed to take place and the location of the jet boundary is correlated differently. Therefore, it is somewhat misleading to compare radial pressure distributions at only a single axial location. Nonetheless, even one such isolated example will serve to illustrate the

significant divergence between the predictions of the two models. Figure I-24 displays the radial pressure distributions at axial distances corresponding to the location of the respective asymptotic planes predicted by the ANSI model. For the more highly subcooled condition, this location is 7.5 break diameters; for the less subcooled state, it occurs at 7.25 break diameters. Although Kastner predicts higher jet centerline pressures, it can be seen that the ANSI model yields a more divergent jet. This follows from two critical physical assumptions inherent in the ANSI model.

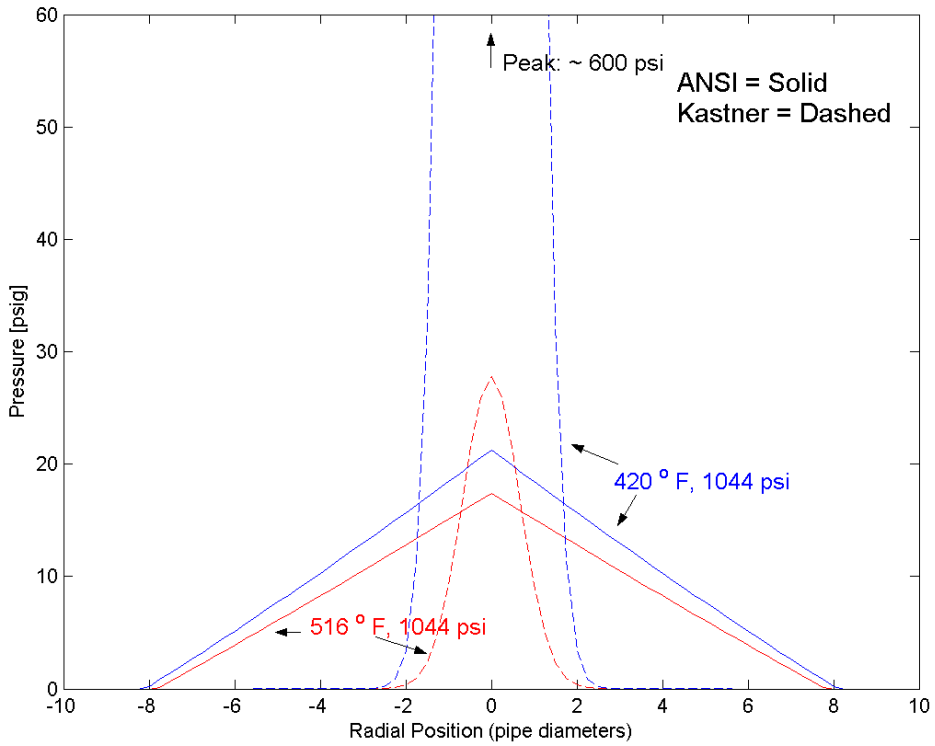

Figure I-24. Radial Impingement Pressure Distribution on a Plate Positioned at the ANSI Model Asymptotic Plane

First, the ANSI model is constrained to preserve the jet mass flow rate (kilogram per second [kg/s]). One might expect some mass to escape from the jet, such that the mass flow rate across a normally oriented plane downstream of the break would be less than the initial flow rate. However, the ANSI model does not allow mass to escape from the jet. Second, the model preserves the initial jet force at all downstream locations; the full force is always recovered on any large normally oriented plate. In fact, four mechanisms leading to downstream recovery of less than the initial force can be identified:

(1) If one envisions a control volume such as that drawn in

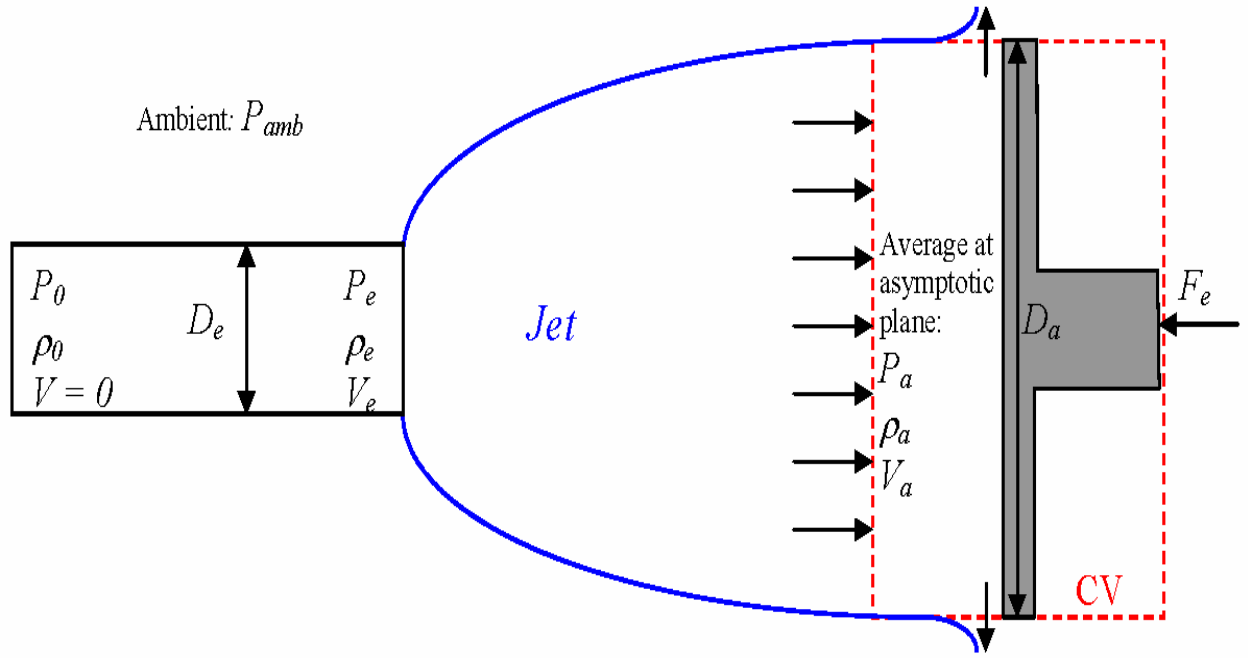

Figure I-4, mass may have departed from the forward-traveling jet and crossed the sides of the control volume before impacting the plate.

(2) Fluid impinging on the plate may have a tangential velocity component that will not contribute to the measured thrust.

(3) Energy transfer via mixing with the environment may occur to some extent dependent on the distance to the target.

(4) Dissipative losses across standing shock boundaries near the targets may be important.

The issue of downstream force recovery may be divided into two components, fraction of initial force recovered and magnitude of initial force. This discussion addressed each separately, with the recovery fraction treated first. Figure I-25 shows the fractional jet thrust force recovery as the downstream location varies from 0 to 10 break diameters. Kastner's correlation implies that significantly less than the full jet force is recovered downstream of the break. These results can be obtained by either numerically or analytically integrating the respective radial pressure profiles for the two models and normalizing by the mass flux present at the break plane. Comparison between the two thermodynamic cases shows that the portion of the initial force that is lost increases as the initial subcooling decreases. The smaller fractional recovery given by the Kastner model may be counterintuitive given that its jet centerline pressure predictions as shown in Figure I-23 and Figure I-24 are greater than that of the ANSI model. However, it must be borne in mind that the recovered force is obtained by computing an integral over the jet impingement area. The ANSI jet, being significantly more dispersed, impinges upon a much larger area; in fact, the area is designed to yield full force recovery and only the definition of the geometric envelope defines the radial extent of the jet cross section.

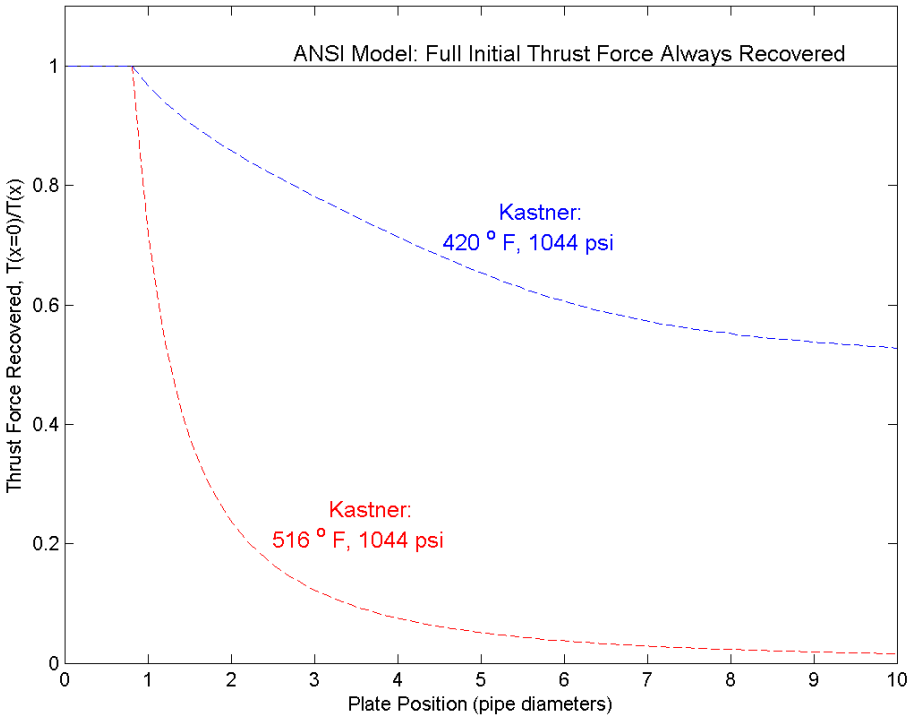

Figure I-25. Fraction of Initial Jet Thrust Force Recovered on Large Normally Oriented Plate, as a Function of Plate Location

The initial thrust force predicted by the ANSI model depends on the method used to compute the discharge mass flow rate (Henry-Fauske was employed here), while the actual flow rate is already embedded in Kastner's experimental results. Hence, the models' initial thrust forces are also different, even for comparable initial conditions. In fact, assuming no resistance in the nozzle, the ANSI model using Henry-Fauske critical flow parameters predicts larger initial thrust forces than the Kastner model. Specifically, the ANSI/Henry-Fauske initial force is 46 percent larger for the less-subcooled condition and 121 percent larger for the more-subcooled state.

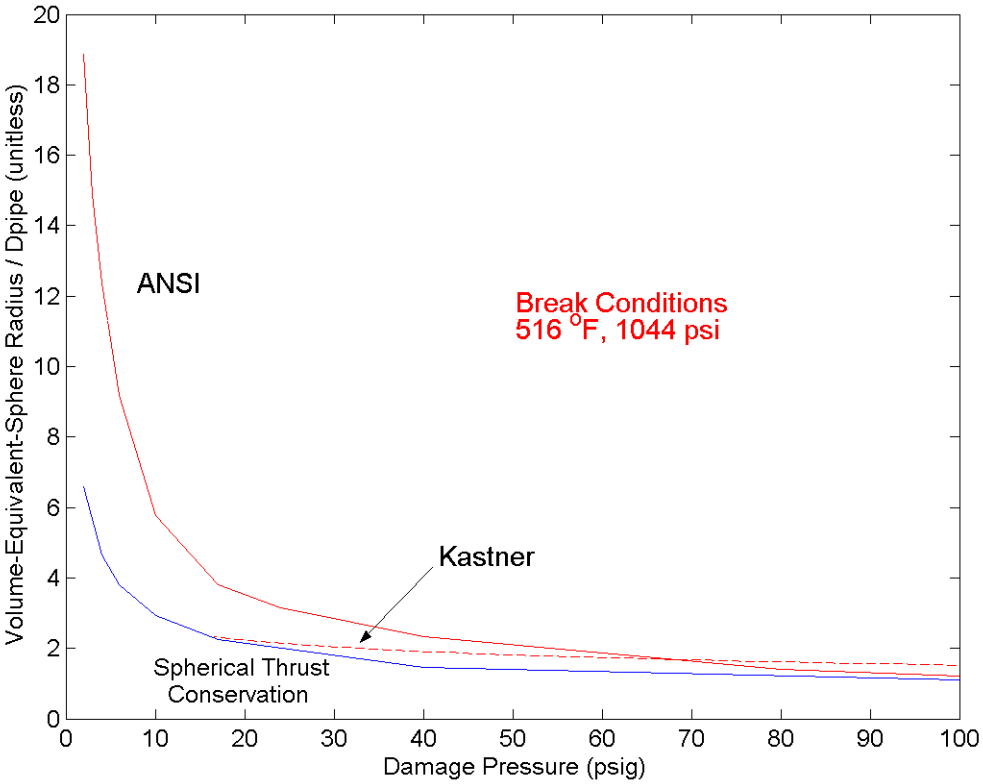

Figure I-26. Comparison of Equivalent Spherical Damage Radii

Figure I-26 presents one comparative metric of great interest for this application, the radius of the volume-equivalent sphere obtained for any given damage pressure. The narrower jet geometry given by the Kastner model leads to smaller radii for all but very high damage pressures. At the highest pressures, differences in the treatment of the area immediately surrounding the core become important. The ANSI model exhibits a large and discontinuous pressure drop as one crosses the core boundary; hence, Kastner's continuous model results in locally higher pressures in this region. The authors of the Kastner model recognize this as a shortcoming of the methodology; however, the correction proposed in KAS88 is only relevant to rectangular orifice geometries and will not be considered here. Also, Kastner's correlation is only fully validated out to a centerline range of 10 pipe diameters, beyond which the pressures fall below 15 psig. Therefore, the dashed line in Figure I-26 is truncated.

The key physical assumption that drives the development of the ANSI model is the conservation of momentum flux across the area of the asymptotic plane. Other considerations define the location and size of this plane, as discussed previously. However, an abstract point source that dissipates energy by geometric attenuation only as it expands isotropically can represent the geometric limit of the momentum conservation approach. The blue line in Figure I-26 illustrates the $1/R^2$ relationship between spherical radius and surface-averaged pressure inherent to the spherical momentum-conservation limit. Physical models based on energy conservation should not yield results below this limit for a given break condition, but empirical data such as Kastner and numerical models that incorporate physical energy losses may yield trends

below the limit. This case is presented to help judge the magnitude of marginal returns that might be realized with respect to ZOI volume by selecting a more realistic jet model.

Generally, the ANSI model, regardless of whether the Henry-Fauske or homogeneous equilibrium critical flow relation is used, yields conservative results when compared to Kastner's correlations—initial thrust forces and downstream force recovery are both larger. Even if the Kastner model is the more accurate, these conservatisms are not entirely unjustified for the present application. First, Kastner's experimental results were universally obtained with nonidealized discharge conditions (i.e., a nonzero hydraulic coefficient of resistance). Although the Kastner model may be compared to the idealized conditions studied here, this represents an extrapolation rather than an interpolation of the experimental results. Furthermore, the present application is not merely concerned with jet impingement on normally oriented structures or on targets located near the jet centerline. For the complicated target geometries that might be encountered within a containment building, volume-equivalent spheres computed using the ANSI model corresponding to a range of impingement pressures provide a conservative approach for computing potential ZOI damage volumes. Hence, pending experimental and/or theoretical investigation of jet stagnation pressures and velocity fields at locations away from the centerline, it seems prudent to impose full jet mass flow and force recovery as preserved by the ANSI model.

I.8 Summary of Examination of the ANSI Jet Model

Appendix I provides an exposition of the ANSI model and addresses several points where the model may be insufficiently clear or may suffer from an inconsistency. The following summarizes the major issues raised in the appendix and provides recommendations for remediation where applicable:

- The pressure distribution produced by the model exhibits a discontinuity across the boundary of the core. Within the core, the stagnation pressure is assumed to equal the upstream pressure P_0; the discontinuity has been observed to reach an order of magnitude for certain upstream conditions.
- Although not explicitly stated in the model, the jet pressure distribution, which falls to zero in the far field, must be interpreted as representative of local impingement gauge pressures.
- The jet pressure at the centerline, however, remains nonzero for any finite value of the axial penetration distance. This exaggerates pressure isobar volumes and causes volume-equivalent spherical damage radii to approach infinity as the damage pressure goes to zero.
- The pressure distribution has evidently been formulated such that the thrust force is correctly recovered only for targets oriented normal to the flow direction at the orifice. Therefore, the model may not be a good approximation to free-field expansion; it may not accurately predict local conditions at points away from the jet centerline, where the flow velocity on such a normally oriented plate would exhibit a significant tangential component. This concern is not addressed by the application of a shape factor, as outlined in Appendix D to the ANSI report.

- The above point has further ramifications for the applicability of the model to small targets. Because the stagnation pressure field produced by the model was developed to reproduce loadings on large flat targets, it is inaccurate to apply the stagnation pressures to small and/or nonflat objects. One could bound the true conditions by computing local static pressures, as well; however, knowledge of the local velocity field and of the characteristics of the two-phase jet flow that are beyond the scope of the ANSI model would be required.
- A discontinuity in the slope of the isobars exists between Zones 2 and 3. Figure I-1 clearly shows this discontinuity. The sharp terminal points of pressure isobars at the axial centerline also suggest that more attention could be given to the behavior of first spatial derivatives.
- The assumption of isentropic and/or isenthalpic expansion should be made with caution. For instance, stagnation conditions at the asymptotic plane are evaluated assuming isenthalpic behavior, implying no energy loss to the environment. In general, however, the isentropic assumption appears to be applied to the expanding jet. For a discussion of the limitations of these assumptions, see WIT02.
- Although it was analytically confirmed that all characteristic lengths in the problem scale linearly with the break diameter, D_e, it is recommended that users implement the formulation of the model presented herein, as it has been nondimensionalized with respect to this quantity.
- The notation adopted by the standard for the thrust coefficient is evidently inconsistent; C_T, C_{Te}, and C^*_{Te} all appear in the equations describing the pressure distribution for the various jet zones. These forms must all refer to a single numeric value if the pressure equations are to be piecewise continuous between zones.
- The ANSI model presents an expression for the jet area at the asymptotic plane that rests upon the assumption that the average flow static pressure at that location equals the ambient pressure, P_{amb}. Elsewhere in the ANSI model, however, the asymptotic plane static pressure is assigned a value that may be less than P_{amb}.
- The standard advises users to implement a critical flow model, either the homogeneous equilibrium model (HEM) or the Henry-Fauske model, to obtain the jet mass flux G_e. Users not having such a model available may estimate G_e from Figure C-4 of the ANSI report; however, this figure only covers stagnation conditions extending to 2000 psi and 50°F of subcooling, leaving certain states (e.g., cold-leg conditions in many PWRs) unaddressed. Given the additional inaccuracies that reading from the figure may introduce, it is strongly recommended that a critical flow model be implemented for use with the jet model.
- The standard recommends that the Henry-Fauske critical flow model be used for subcooled vessel conditions and the HEM for saturated conditions. This would introduce a strong discontinuity as the liquid saturation point is crossed. Therefore, because Henry-Fauske is evidently in better agreement with the

data for both subcooled and two-phase conditions, exclusive use of this model is recommended.

- An implied discontinuity exists across the break plane, as the ANSI model assumes that fluid in the core is in equilibrium at the upstream stagnation pressure and quality. This assumption contradicts aspects of both the HEM and the Henry-Fauske models.
- The correlation recommended by the standard for use in calculating the thrust coefficient, C_T, for subcooled conditions applies only to Henry-Fauske derived mass fluxes. The standard does not make this clear. In addition, it left unclear the assumption inherent in the correlation that ambient conditions are at standard pressure. Therefore, this correlation should not be used in conjunction with HEM mass fluxes, and users of the standard should bear in mind that the correlation is not strictly validated for ambient conditions deviating from those of the standard atmosphere. The error is small, though, for most upstream pressures of interest in the present analysis.
- The standard provides no analytic correlation for the thrust coefficient relevant to saturated steam-water mixtures. Within the standard, users may only consult Figure B-5 to visually gauge an approximate value. Another recourse would be to consult the thrust coefficient contour plots presented in this appendix or, better, implement a critical mass flux model to enable direct calculation of mass flux and thrust coefficient via the Henry-Fauske model.
- Users should be aware that one desired result of the model, volume-equivalent spherical damage-pressure radii, can behave nonintuitively as certain upstream conditions are varied. For instance, the PWR hot-leg and cold-leg results presented in Table I-1 of this appendix show that the flow from the hot-leg break exhibits a lower mass flux and thrust coefficient than that from the cold leg. Nonetheless, the damage radii are roughly comparable, with radii for the hot-leg break exceeding those of the cold leg for higher damage pressures and smaller for lower damage pressures. These results, which follow from variations in the flow velocity and density at the break, reinforce the importance of not eliminating lower energy break points *a priori* when conducting ZOI analyses.

I.9 References

ANS88 "American National Standard: Design Basis for Protection of Light Water Nuclear Power Plants Against the Effects of Postulated Pipe Rupture," American Nuclear Society, ANSI/ANS-58.2-1988, October 1988.

DUD76 Duderstadt, J.J. and L.J. Hamilton, *Nuclear Reactor Analysis*, Wiley and Sons, New York, New York, 1976.

HAL80 Hall, D.G. and L.S. Czapary, "Tables of Homogeneous Equilibrium Critical Flow Parameters for Water in SI Units," EG&G Idaho Report EGG-2056, 1980.

HAR96 Harvey, A.H., A.P. Peskin, and S.A. Klein, "NIST/ASME Steam Properties: Formulation for General and Scientific Use," Version 2.11, 1996.

HEN71 Henry, R.E. and H.K. Fauske, "The Two Phase Critical Flow of One-Component Mixtures in Nozzles, Orifices, and Short Tubes," *J. Heat Transfer*, p. 179, May 1971.

KAS88 Kastner, W. and R. Rippel, "The Two Phase Critical Flow of One-Component Mixtures in Nozzles, Orifices, and Short Tubes," *Nucl. Engr. and Design*, 105, p. 269, 1988.

LAH84 Lahey, R.T. and F.J. Moody, *The Thermal-Hydraulics of a Boiling Water Nuclear Reactor*, 3rd ed., La Grande Park, IL: ANS Press, p. 381, 1984.

LOB90 Lobner, P., C. Donahoe, and C. Cavallin, "Overview and Comparison of U.S. Commercial Nuclear Power Plants," prepared for the U.S. Nuclear Regulatory Commission by Science Applications International Corporation, NUREG/CR-5640, SAIC-89/1541, September 1990.

NEI04 "Pressurized-Water-Reactor Sump Performance Evaluation Methodology," Nuclear Energy Institute, May 28, 2004.

NRC98 "Safety Evaluation by the Office of Nuclear Reactor Regulation Related to NRC Bulletin 96-03, Boiling Water Reactor Owners Group Topical Report NEDO-32686," U.S. Nuclear Regulatory Commission, August 1998.

NRC03 Regulatory Guide 1.82, Rev. 3, "Water Sources for Long-Term Recirculation Cooling Following a Loss-of-Coolant Accident," U.S. Nuclear Regulatory Commission, Office of Nuclear Regulatory Research, August 2003.

RAH92 Rahn, F.J., et al., *Guide to Nuclear Power Technology: A Resource for Decision Making*, Krieger, Malabar, FL, 1992.

RAO02 Rao, D.V., K.W. Ross, and S.G. Ashbaugh, "GSI-191: Thermal-Hydraulic Response of PWR Reactor Coolant System and Containments

to Selected Accident Sequences," prepared for the U.S. Nuclear Regulatory Commission by Los Alamos National Laboratory, NUREG/CR-6770, LA-UR-01-5561, August 2002.

URG96 NEDO-32686, Rev. 0, "Utility Resolution Guidance for ECCS Strainer Blockage," General Electric Nuclear Energy Company, Class 1, November 1996.

WEB76 Webb, S.W., "Evaluation of Subcooled Water Thrust Forces," *Nucl. Technology*, Vol. 31, p. 48, October 1976.

WEI83 Weigand, G.G., et al., "Two-Phase Jet Loads," NUREG/CR-2913, prepared for the U.S. Nuclear Regulatory Commission by Sandia National Laboratory, January 1983.

WIT02 Witlox, H.W. and P.J. Bowen, "Flashing Liquid Jets and Two-Phase Dispersion: A Review," United Kingdom Health and Safety Executive Contract Research Report 403/2002, p. 37, 2002.